UNIVERSITY OF AMSTERDAM

UvA-DARE (Digital Academic Repository)

Photon reconstruction in the ATLAS inner detector and liquid argon barrel calorimeter at the 2004 combined test beam

Abat, E.; et al., [Unknown]; Ferrari, P.; Gorfine, G.; Liebig, W.

[Link to publication](#)

Photon reconstruction in the ATLAS Inner Detector and Liquid Argon Barrel Calorimeter at the 2004 Combined Test Beam

Photon reconstruction in the ATLAS Inner Detector and Liquid Argon Barrel Calorimeter at the 2004 Combined Test Beam

E. Abat,[k,1] J.M. Abdallah,[f] T.N. Addy,[ag] P. Adragna,[cc] M. Aharrouche,[ba]
A. Ahmad,[cm,2] T.P.A. Akesson,[ay] M. Aleksa,[s] C. Alexa,[n] K. Anderson,[t]
A. Andreazza,[be,bf] F. Anghinolfi,[s] A. Antonaki,[e] G. Arabidze,[e] E. Arik,[k] T. Atkinson,[bd]
J. Baines,[cf] O.K. Baker,[dd] D. Banfi,[be,bf] S. Baron,[s] A.J. Barr,[bs] R. Beccherle,[aj]
H.P. Beck,[i] B. Belhorma,[aw] P.J. Bell,[bb,3] D. Benchekroun,[q] D.P. Benjamin,[ac]
K. Benslama,[cg] E. Bergeaas Kuutmann,[cp,4] J. Bernabeu,[cz] H. Bertelsen,[v] S. Binet,[bq]
C. Biscarat,[ad] V. Boldea,[n] V.G. Bondarenko,[bk] M. Boonekamp,[cj] M. Bosman,[f]
C. Bourdarios,[bq] Z. Broklova,[ca] D. Burckhart Chromek,[s] V. Bychkov,[an] J. Callahan,[ai]
D. Calvet,[u] M. Canneri,[bw] M. Capeáns Garrido,[s] M. Caprini,[n] L. Cardiel Sas,[s]
T. Carli,[s] L. Carminati,[be,bf] J. Carvalho,[p,by] M. Cascella,[bw] M.V. Castillo,[cz]
A. Catinaccio,[s] D. Cauz,[ak] D. Cavalli,[be] M. Cavalli Sforza,[f] V. Cavasinni,[bw]
S.A. Cetin,[k] H. Chen,[j] R. Cherkaoui,[cd] L. Chevalier,[cj] F. Chevallier,[aw] S. Chouridou,[cx]
M. Ciobotaru,[cv] M. Citterio,[be] A. Clark,[ae] B. Cleland,[bx] M. Cobal,[ak] E. Cogneras,[i]
P. Conde Muino,[by] M. Consonni,[be,bf] S. Constantinescu,[n] T. Cornelissen,[s,5]
S. Correard,[w] A. Corso Radu,[s] G. Costa,[be] M.J. Costa,[cz] D. Costanzo,[cl] S. Cuneo,[aj]
P. Cwetanski,[ai] D. Da Silva,[ch] M. Dam,[v] M. Dameri,[aj] H.O. Danielsson,[s]
D. Dannheim,[s] G. Darbo,[aj] T. Davidek,[ca] K. De,[d] P.O. Defay,[u] B. Dekhissi,[ax] J. Del
Peso,[az] T. Del Prete,[bw] M. Delmastro,[s] F. Derue,[av] L. Di Ciaccio,[ar] B. Di Girolamo,[s]
S. Dita,[n] F. Dittus,[s] F. Djama,[w] T. Djobava,[cs] D. Dobos,[aa,6] M. Dobson,[s]
B.A. Dolgoshein,[bk] A. Dotti,[bw] G. Drake,[b] Z. Drasal,[ca] N. Dressnandt,[bu] C. Driouchi,[v]
J. Drohan,[cw] W.L. Ebenstein,[ac] P. Eerola,[ay,7] I. Efthymiopoulos,[s] K. Egorov,[ai]

---

[1] Deceased.

[2] Now at SUNY, Stony Brook U.S.A.

[3] Now at Université de Genève, Geneva Switzerland.

[4] Now at DESY, Zeuthen Germany.

[5] Now at INFN Genova and Università di Genova, Genova Italy.

[6] Now at CERN, Geneva Switzerland.

[7] Now at University of Helsinki, Helsinki Finland.

T.F. Eifert,[s] K. Einsweiler,[h] M. El Kacimi,[as] M. Elsing,[s] D. Emelyanov,[cf,8] C. Escobar,[cz]
A.I. Etienvre,[cj] A. Fabich,[s] K. Facius,[v] A.I. Fakhr-Edine,[o] M. Fanti,[be,bf] A. Farbin,[d]
P. Farthouat,[s] D. Fassouliotis,[e] L. Fayard,[bq] R. Febbraro,[u] O.L. Fedin,[bv] A. Fenyuk,[cb]
D. Fergusson,[h] P. Ferrari,[s,9] R. Ferrari,[bt] B.C. Ferreira,[ch] A. Ferrer,[cz] D. Ferrere,[ae]
G. Filippini,[u] T. Flick,[dc] D. Fournier,[bq] P. Francavilla,[bw] D. Francis,[s] R. Froeschl,[s,10]
D. Froidevaux,[s] E. Fullana,[b] S. Gadomski,[ae] G. Gagliardi,[aj] P. Gagnon,[ai] M. Gallas,[s]
B.J. Gallop,[cf] S. Gameiro,[s] K.K. Gan,[bp] R. Garcia,[az] C. Garcia,[cz] I.L. Gavrilenko,[bj]
C. Gemme,[aj] P. Gerlach,[dc] N. Ghodbane,[u] V. Giakoumopoulou,[e] V. Giangiobbe,[bw]
N. Giokaris,[e] G. Glonti,[an] T. Goettfert,[bm] T. Golling,[h,10] N. Gollub,[s] A. Gomes,[at,au,by]
M.D. Gomez,[ae] S. Gonzalez-Sevilla,[cz,3] M.J. Goodrick,[r] G. Gorfine,[bo] B. Gorini,[s]
D. Goujdami,[o] K-J. Grahn,[aq] P. Grenier,[u,11] N. Grigalashvili,[an] Y. Grishkevich,[bl]
J. Grosse-Knetter,[l,12] M. Gruwe,[s] C. Guicheney,[u] A. Gupta,[t] C. Haeberli,[i]
R. Haertel,[bm,13] Z. Hajduk,[y] H. Hakobyan,[de] M. Hance,[bu] J.D. Hansen,[v] P.H. Hansen,[v]
K. Hara,[cu] A. Harvey Jr.,[ag] R.J. Hawkings,[s] F.E.W. Heinemann,[bs] A. Henriques
Correia,[s] T. Henss,[dc] L. Hervas,[s] E. Higon,[cz] J.C. Hill,[r] J. Hoffman,[z] J.Y. Hostachy,[aw]
I. Hruska,[ca] F. Hubaut,[w] F. Huegging,[l] W. Hulsbergen,[s,9] M. Hurwitz,[t]
L. Iconomidou-Fayard,[bq] E. Jansen,[ce] I. Jen-La Plante,[t] P.D.C. Johansson,[cl]
K. Jon-And,[cp] M. Joos,[s] S. Jorgensen,[f] J. Joseph,[h] A. Kaczmarska,[y,14] M. Kado,[bq]
A. Karyukhin,[cb] M. Kataoka,[s,15] F. Kayumov,[bj] A. Kazarov,[bv] P.T. Keener,[bu]
G.D. Kekelidze,[an] N. Kerschen,[cl] S. Kersten,[dc] A. Khomich,[bc] G. Khoriauli,[an]
E. Khramov,[an] A. Khristachev,[bv] J. Khubua,[an] T.H. Kittelmann,[v,16] R. Klingenberg,[aa]
E.B. Klinkby,[ac] P. Kodys,[ca] T. Koffas,[s] S. Kolos,[cv] S.P. Konovalov,[bj]
N. Konstantinidis,[cw] S. Kopikov,[cb] I. Korolkov,[f] V. Kostyukhin,[aj,17] S. Kovalenko,[bv]
T.Z. Kowalski,[x] K. Krüger,[s,18] V. Kramarenko,[bl] L.G. Kudin,[bv] Y. Kulchitsky,[bi]
C. Lacasta,[cz] R. Lafaye,[ar] B. Laforge,[av] W. Lampl,[c] F. Lanni,[j] S. Laplace,[ar] T. Lari,[be]
A-C. Le Bihan,[s,19] M. Lechowski,[bq] F. Ledroit-Guillon,[aw] G. Lehmann,[s] R. Leitner,[ca]
D. Lelas,[bq] C.G. Lester,[r] Z. Liang,[z] P. Lichard,[s] W. Liebig,[bo] A. Lipniacka,[g]
M. Lokajicek,[bz] L. Louchard,[u] K.F. Loureiro,[bp] A. Lucotte,[aw] F. Luehring,[ai]
B. Lund-Jensen,[aq] B. Lundberg,[ay] H. Ma,[j] R. Mackeprang,[v] A. Maio,[at,au,by]

[8] Now at Joint Institute for Nuclear Research, Dubna Russia.
[9] Now at Nikhef National Institute for Subatomic Physics, Amsterdam Netherlands.
[10] Now at Yale University, New Haven U.S.A.
[11] Now at SLAC, Stanford U.S.A.
[12] Now at Georg-August-Universität, Göttingen Germany.
[13] Now at Versicherungskammer Bayern, Munich Germany.
[14] Now at Université Pierre et Marie Curie (Paris 6) and Université Denis Diderot (Paris-7), Paris France.
[15] Now at Laboratoire de Physique de Particules (LAPP), Annecy-le-Vieux France.
[16] Now at University of Pittsburgh, Pittsburgh U.S.A.
[17] Now at Physikalisches Institut der Universität Bonn, Bonn Germany.
[18] Now at Universität Heidelberg, Heidelberg Germany.
[19] Now at IPHC, Université de Strasbourg, CNRS/IN2P3, Strasbourg France.

V.P. Maleev,[bv] **F. Malek,**[aw] **L. Mandelli,**[be] **J. Maneira,**[by] **M. Mangin-Brinet,**[ae,20]
A. Manousakis,[e] **L. Mapelli,**[s] **C. Marques,**[by] **S.Marti i Garcia,**[cz] **F. Martin,**[bu]
M. Mathes,[l] **M. Mazzanti,**[be] **K.W. McFarlane,**[ag] **R. McPherson,**[da] **G. Mchedlidze,**[cs]
S. Mehlhase,[ah] **C. Meirosu,**[s] **Z. Meng,**[ck] **C. Meroni,**[be] **V. Mialkovski,**[an] **B. Mikulec,**[ae,6]
D. Milstead,[cp] **I. Minashvili,**[an] **B. Mindur,**[x] **V.A. Mitsou,**[cz] **S. Moed,**[ae,21] **E. Monnier,**[w]
G. Moorhead,[bd] **P. Morettini,**[aj] **S.V. Morozov,**[bk] **M. Mosidze,**[cs] **S.V. Mouraviev,**[bj]
E.W.J. Moyse,[s] **A. Munar,**[bu] **A. Myagkov,**[cb] **A.V. Nadtochi,**[bv] **K. Nakamura,**[cu,22]
P. Nechaeva,[aj,23] **A. Negri,**[bt] **S. Nemecek,**[bz] **M. Nessi,**[s] **S.Y. Nesterov,**[bv]
F.M. Newcomer,[bu] **I. Nikitine,**[cb] **K. Nikolaev,**[an] **I. Nikolic-Audit,**[av] **H. Ogren,**[ai] **S.H. Oh,**[ac]
S.B. Oleshko,[bv] **J. Olszowska,**[y] **A. Onofre,**[bg,by] **C. Padilla Aranda,**[s] **S. Paganis,**[cl,24]
D. Pallin,[u] **D. Pantea,**[n] **V. Paolone,**[bx] **F. Parodi,**[aj] **J. Parsons,**[bn] **S. Parzhitskiy,**[an]
E. Pasqualucci,[ci] **S.M. Passmored,**[s] **J. Pater,**[bb] **S. Patrichev,**[bv] **M. Peez,**[az] **V. Perez
Reale,**[bn] **L. Perini,**[be,bf] **V.D. Peshekhonov,**[an] **J. Petersen,**[s] **T.C. Petersen,**[v] **R. Petti,**[j,25]
P.W. Phillips,[cf] **J. Pilcher,**[t] **J. Pina,**[at,au,by] **B. Pinto,**[by] **F. Podlyski,**[u] **L. Poggioli,**[bq]
A. Poppleton,[s] **J. Poveda,**[db] **P. Pralavorio,**[w] **L. Pribyl,**[s] **M.J. Price,**[s] **D. Prieur,**[cf]
C. Puigdengoles,[f] **P. Puzo,**[bq] **F. Ragusa,**[be,bf] **S. Rajagopalan,**[j] **K. Reeves,**[dc,26]
I. Reisinger,[aa] **C. Rembser,**[s] **P.A.Bruckman.de. Renstrom,**[bs] **P. Reznicek,**[ca] **M. Ridel,**[av]
P. Risso,[aj] **I. Riu,**[ae,27] **D. Robinson,**[r] **C. Roda,**[bw] **S. Roe,**[s] **O. Røhne,**[br] **A. Romaniouk,**[bk]
D. Rousseau,[bq] **A. Rozanov,**[w] **A. Ruiz,**[cz] **N. Rusakovich,**[an] **D. Rust,**[ai] **Y.F. Ryabov,**[bv]
V. Ryjov,[s] **O. Salto,**[f] **B. Salvachua,**[b] **A. Salzburger,**[al,6] **H. Sandaker,**[g] **C. Santamarina
Rios,**[s] **L. Santi,**[ak] **C. Santoni,**[u] **J.G. Saraiva,**[at,au,by] **F. Sarri,**[bw] **G. Sauvage,**[ar] **L.P. Says,**[u]
M. Schaefer,[aw] **V.A. Schegelsky,**[bv] **C. Schiavi,**[aj] **J. Schieck,**[bm] **G. Schlager,**[s]
J. Schlereth,[b] **C. Schmitt,**[ba] **J. Schultes,**[dc] **P. Schwemling,**[av] **J. Schwindling,**[cj]
J.M. Seixas,[ch] **D.M. Seliverstov,**[bv] **L. Serin,**[bq] **A. Sfyrla,**[ae,6] **N. Shalanda,**[bh] **C. Shaw,**[af]
T. Shin,[ag] **A. Shmeleva,**[bj] **J. Silva,**[by] **S. Simion,**[bq] **M. Simonyan,**[ar] **J.E. Sloper,**[s]
S.Yu. Smirnov,[bk] **L. Smirnova,**[bl] **C. Solans,**[cz] **A. Solodkov,**[cb] **O. Solovianov,**[cb]
I. Soloviev,[bv] **V.V. Sosnovtsev,**[bk] **F. Spanò,**[bn] **P. Speckmayer,**[s] **S. Stancu,**[cv] **R. Stanek,**[b]
E. Starchenko,[cb] **A. Straessner,**[ab] **S.I. Suchkov,**[bk] **M. Suk,**[ca] **R. Szczygiel,**[x]
F. Tarrade,[j] **F. Tartarelli,**[be] **P. Tas,**[ca] **Y. Tayalati,**[u] **F. Tegenfeldt,**[am] **R. Teuscher,**[ct]
M. Thioye,[cq] **V.O. Tikhomirov,**[bj] **C.J.W.P. Timmermans,**[ce] **S. Tisserant,**[w] **B. Toczek,**[x]
L. Tremblet,[s] **C. Troncon,**[be] **P. Tsiareshka,**[bi] **M. Tyndel,**[cf] **M.Karagoez. Unel,**[bs]
G. Unal,[s] **G. Unel,**[ai] **G. Usai,**[t] **R. Van Berg,**[bu] **A. Valero,**[cz] **S. Valkar,**[ca] **J.A. Valls,**[cz]
W. Vandelli,[s] **F. Vannucci,**[av] **A. Vartapetian,**[d] **V.I. Vassilakopoulos,**[ag] **L. Vasilyeva,**[bj]

[20]Now at Laboratoire de Physique Subatomique et de Cosmologie CNRS/IN2P3, Grenoble France.

[21]Now at Harvard University, Cambridge U.S.A.

[22]Now at ICEPP, Tokyo Japan.

[23]Now at P.N. Lebedev Institute of Physics, Moscow Russia.

[24]Corresponding author.

[25]Now at University of South Carolina, Columbia U.S.A.

[26]Now at UT Dallas, Dallas U.S.A.

[27]Now at IFAE, Barcelona Spain.

F. Vazeille,[u] **F. Vernocchi,**[aj] **Y. Vetter-Cole,**[z] **I. Vichou,**[cy] **V. Vinogradov,**[an] **J. Virzi,**[h]
I. Vivarelli,[bw] **J.B.de. Vivie,**[w,28] **M. Volpi,**[f] **T. Vu Anh,**[ae,29] **C. Wang,**[ac] **M. Warren,**[cw]
J. Weber,[aa] **M. Weber,**[cf] **A.R. Weidberg,**[bs] **J. Weingarten,**[l,12] **P.S. Wells,**[s] **P. Werner,**[s]
S. Wheeler,[a] **M. Wiessmann,**[bm] **H. Wilkens,**[s] **H.H. Williams,**[bu] **I. Wingerter-Seez,**[ar]
Y. Yasu,[ap] **A. Zaitsev,**[cb] **A. Zenin,**[cb] **T. Zenis,**[m] **Z. Zenonos,**[bw] **H. Zhang,**[w] **A. Zhelezko**[bk]
and N. Zhou[bn]

[a]*University of Alberta, Department of Physics, Centre for Particle Physics,*
 Edmonton, AB T6G 2G7, Canada

[b]*Argonne National Laboratory, High Energy Physics Division,*
 9700 S. Cass Avenue, Argonne IL 60439, U.S.A.

[c]*University of Arizona, Department of Physics,*
 Tucson, AZ 85721, U.S.A.

[d]*University of Texas at Arlington, Department of Physics,*
 Box 19059, Arlington, TX 76019, U.S.A.

[e]*University of Athens, Nuclear & Particle Physics Department of Physics,*
 Panepistimiopouli Zografou, GR 15771 Athens, Greece

[f]*Institut de Fisica d'Altes Energies, IFAE, Universitat Autònoma de Barcelona,*
 Edifici Cn, ES-08193 Bellaterra (Barcelona) Spain

[g]*University of Bergen, Department for Physics and Technology,*
 Allegaten 55, NO-5007 Bergen, Norway

[h]*Lawrence Berkeley National Laboratory and University of California, Physics Division,*
 MS50B-6227, 1 Cyclotron Road, Berkeley, CA 94720, U.S.A.

[i]*University of Bern, Laboratory for High Energy Physics,*
 Sidlerstrasse 5, CH-3012 Bern, Switzerland

[j]*Brookhaven National Laboratory, Physics Department,*
 Bldg. 510A, Upton, NY 11973, U.S.A.

[k]*Bogazici University, Faculty of Sciences, Department of Physics,*
 TR-80815 Bebek-Istanbul, Turkey

[l]*Physikalisches Institut der Universitaet Bonn,*
 Nussallee 12, D-53115 Bonn, Germany

[m]*Comenius University, Faculty of Mathematics Physics & Informatics,*
 Mlynska dolina F2, SK-84248 Bratislava, Slovak Republic

[n]*National Institute of Physics and Nuclear Engineering (Bucharest -IFIN-HH),*
 P.O. Box MG-6, R-077125 Bucharest, Romania

[o]*Université Cadi Ayyad,*
 Marrakech, Morocco

[p]*Department of Physics, University of Coimbra,*
 P-3004-516 Coimbra, Portugal

[q]*Université Hassan II, Faculté des Sciences Ain Chock,*
 B.P. 5366, MA-Casablanca, Morocco

[r]*Cavendish Laboratory, University of Cambridge,*
 J.J. Thomson Avenue, Cambridge CB3 0HE, U.K.

---

[28]Now at LAL-Orsay, Orsay France.

[29]Now at Universität Mainz, Mainz Germany.

^{s} *European Laboratory for Particle Physics (CERN),*
  CH-1211 Geneva 23, Switzerland

^{t} *University of Chicago, Enrico Fermi Institute,*
  5640 S. Ellis Avenue, Chicago, IL 60637, U.S.A.

^{u} *Laboratoire de Physique Corpusculaire (LPC), IN2P3-CNRS, Université Blaise-Pascal,*
  Clermont-Ferrand, FR-63177 Aubiere, France

^{v} *Niels Bohr Institute, University of Copenhagen,*
  Blegdamsvej 17, DK-2100 Kobenhavn 0, Denmark

^{w} *Université Méditerranée, Centre de Physique des Particules de Marseille, CNRS/IN2P3,*
  F-13288 Marseille, France

^{x} *Faculty of Physics and Applied Computer Science of the AGH-University of Science and Technology,*
  (FPACS, AGH-UST),
  al. Mickiewicza 30, PL-30059 Cracow, Poland

^{y} *The Henryk Niewodniczanski Institute of Nuclear Physics, Polish Academy of Sciences,*
  ul. Radzikowskiego 152, PL-31342 Krakow Poland

^{z} *Southern Methodist University, Physics Department,*
  106 Fondren Science Building, Dallas, TX 75275-0175, U.S.A.

^{aa} *Universitaet Dortmund, Experimentelle Physik IV,*
  DE-44221 Dortmund, Germany

^{ab} *Technical University Dresden, Institut fuer Kern- und Teilchenphysik,*
  Zellescher Weg 19, D-01069 Dresden, Germany

^{ac} *Duke University, Department of Physics,*
  Durham, NC 27708, U.S.A.

^{ad} *Centre de Calcul CNRS/IN2P3,*
  Lyon, France

^{ae} *Université de Genève, section de Physique,*
  24 rue Ernest Ansermet, CH-1211 Genève 4, Switzerland

^{af} *University of Glasgow, Department of Physics and Astronomy,*
  Glasgow G12 8QQ, U.K.

^{ag} *Hampton University, Department of Physics,*
  Hampton, VA 23668, U.S.A.

^{ah} *Institute of Physics, Humboldt University, Berlin,*
  Newtonstrasse 15, D-12489 Berlin, Germany

^{ai} *Indiana University, Department of Physics,*
  Swain Hall West 117, Bloomington, IN 47405-7105, U.S.A.

^{aj} *INFN Genova and Università di Genova, Dipartimento di Fisica,*
  via Dodecaneso 33, IT-16146 Genova, Italy

^{ak} *INFN Gruppo Collegato di Udine and Università di Udine, Dipartimento di Fisica,*
  via delle Scienze 208, IT-33100 Udine, Italy and
  INFN Gruppo Collegato di Udine and ICTP,
  Strada Costiera 11, IT-34014 Trieste, Italy

^{al} *Institut fuer Astro- und Teilchenphysik,*
  Technikerstrasse 25, A-6020 Innsbruck, Austria

^{am} *Iowa State University, Department of Physics and Astronomy, Ames High Energy Physics Group,*
  Ames, IA 50011-3160, U.S.A.

^{an} *Joint Institute for Nuclear Research, JINR Dubna,*
  RU-141 980 Moscow Region, Russia

^{ao} *Institut fuer Prozessdatenverarbeitung und Elektronik, Karlsruher Institut fuer Technologie,*
  Campus Nord, Hermann-v.Helmholtz-Platz 1, D-76344 Eggenstein-Leopoldshafen, Germany

^{ap} *KEK, High Energy Accelerator Research Organization,*
  1-1 Oho Tsukuba-shi, Ibaraki-ken 305-0801, Japan

^{aq} *Royal Institute of Technology (KTH), Physics Department,*
  SE-106 91 Stockholm, Sweden

^{ar} *Laboratoire de Physique de Particules (LAPP), Université de Savoie, CNRS/IN2P3,*
  Annecy-le-Vieux Cedex, France

^{as} *Laboratoire de Physique de Particules (LAPP), Université de Savoie, CNRS/IN2P3,*
  Annecy-le-Vieux Cedex, France and
  Université Cadi Ayyad,
  Marrakech, Morocco

^{at} *Departamento de Fisica, Faculdade de Ciências, Universidade de Lisboa,*
  P-1749-016 Lisboa, Portugal

^{au} *Centro de Física Nuclear da Universidade de Lisboa,*
  P-1649-003 Lisboa, Portugal

^{av} *Université Pierre et Marie Curie (Paris 6) and Université Denis Diderot (Paris-7),*
  Laboratoire de Physique Nucléaire et de Hautes Energies, CNRS/IN2P3,
  Tour 33 4 place Jussieu, FR-75252 Paris Cedex 05, France

^{aw} *Laboratoire de Physique Subatomique et de Cosmologie CNRS/IN2P3, Université Joseph Fourier INPG,*
  53 avenue des Martyrs, FR-38026 Grenoble Cedex, France

^{ax} *Laboratoire de Physique Théorique et de Physique des Particules, Université Mohammed Premier,*
  Oujda, Morocco

^{ay} *Lunds universitet, Naturvetenskapliga fakulteten, Fysiska institutionen,*
  Box 118, SE-221 00, Lund, Sweden

^{az} *Universidad Autonoma de Madrid, Facultad de Ciencias, Departamento de Fisica Teorica,*
  ES-28049 Madrid, Spain

^{ba} *Universität Mainz, Institut für Physik,*
  Staudinger Weg 7, DE-55099, Germany

^{bb} *School of Physics and Astronomy, University of Manchester,*
  Manchester M13 9PL, U.K.

^{bc} *Universitaet Mannheim, Lehrstuhl fuer Informatik V,*
  B6, 23-29, DE-68131 Mannheim, Germany

^{bd} *School of Physics, University of Melbourne,*
  AU-Parkvill, Victoria 3010, Australia

^{be} *INFN Sezione di Milano,*
  via Celoria 16, IT-20133 Milano, Italy

^{bf} *Università di Milano, Dipartimento di Fisica,*
  via Celoria 16, IT-20133 Milano, Italy

^{bg} *Departamento de Fisica, Universidade do Minho,*
  P-4710-057 Braga, Portugal

^{bh} *B.I. Stepanov Institute of Physics, National Academy of Sciences of Belarus,*
  Independence Avenue 68, Minsk 220072, Republic of Belarus

^{bi}B.I. Stepanov Institute of Physics, National Academy of Sciences of Belarus,
Independence Avenue 68, Minsk 220072, Republic of Belarus and
Joint Institute for Nuclear Research, JINR Dubna,
RU-141 980 Moscow Region, Russia

^{bj}P.N. Lebedev Institute of Physics, Academy of Sciences,
Leninsky pr. 53, RU-117 924, Moscow, Russia

^{bk}Moscow Engineering & Physics Institute (MEPhI),
Kashirskoe Shosse 31, RU-115409 Moscow, Russia

^{bl}Lomonosov Moscow State University, Skobeltsyn Institute of Nuclear Physics,
RU-119 991 GSP-1 Moscow Lenskiegory 1-2, Russia

^{bm}Max-Planck-Institut für Physik, (Werner-Heisenberg-Institut),
Föhringer Ring 6, 80805 München, Germany

^{bn}Columbia University, Nevis Laboratory,
136 So. Broadway, Irvington, NY 10533, U.S.A.

^{bo}Nikhef National Institute for Subatomic Physics,
Kruislaan 409, P.O. Box 41882, NL-1009 DB Amsterdam, Netherlands

^{bp}Ohio State University,
191 West WoodruAve, Columbus, OH 43210-1117, U.S.A.

^{bq}LAL, Université Paris-Sud, IN2P3/CNRS,
Orsay, France

^{br}University of Oslo, Department of Physics,
P.O. Box 1048, Blindern T, NO-0316 Oslo, Norway

^{bs}Department of Physics, Oxford University,
Denys Wilkinson Building, Keble Road, Oxford OX1 3RH, U.K.

^{bt}Università di Pavia, Dipartimento di Fisica Nucleare e Teorica and INFN Pavia,
Via Bassi 6 IT-27100 Pavia, Italy

^{bu}University of Pennsylvania, Department of Physics, High Energy Physics,
209 S. 33rd Street Philadelphia, PA 19104, U.S.A.

^{bv}Petersburg Nuclear Physics Institute,
RU-188 300 Gatchina, Russia

^{bw}Università di Pisa, Dipartimento di Fisica E. Fermi and INFN Pisa,
Largo B.Pontecorvo 3, IT-56127 Pisa, Italy

^{bx}University of Pittsburgh, Department of Physics and Astronomy,
3941 O'Hara Street, Pittsburgh, PA 15260, U.S.A.

^{by}Laboratorio de Instrumentacao e Fisica Experimental de Particulas — LIP,
and SIM/Univ. de Lisboa,
Avenida Elias Garcia 14-1, PT-1000-149, Lisboa, Portugal

^{bz}Academy of Sciences of the Czech Republic, Institute of Physics and Institute for Computer Science,
Na Slovance 2, CZ-18221 Praha 8, Czech Republic

^{ca}Charles University in Prague, Faculty of Mathematics and Physics, Institute of Particle and Nuclear
Physics,
V Holesovickach 2, CZ-18000 Praha 8, Czech Republic

^{cb}Institute for High Energy Physics (IHEP), Federal Agency of Atom. Energy, Moscow Region,
RU-142 284 Protvino, Russia

^{cc}Queen Mary, University of London,
Mile End Road, E1 4NS, London, U.K.

[cd] Université Mohammed V, Faculté des Sciences,
BP 1014, MO-Rabat, Morocco

[ce] Radboud University Nijmegen/NIKHEF, Dept. of Exp. High Energy Physics,
Toernooiveld 1, NL-6525 ED Nijmegen, Netherlands

[cf] Rutherford Appleton Laboratory, Science and Technology Facilities Council,
Harwell Science and Innovation Campus, Didcot OX11 0QX, U.K.

[cg] University of Regina, Physics Department,
Wascana Parkway, Regina, SK, S4S 0A2, Canada

[ch] Universidade Federal do Rio De Janeiro, Instituto de Fisica,
Caixa Postal 68528, Ilha do Fundao, BR-21945-970 Rio de Janeiro, Brazil

[ci] Università La Sapienza, Dipartimento di Fisica and INFN Roma I,
Piazzale A. Moro 2, IT- 00185 Roma, Italy

[cj] Commissariàt a l'Enegie Atomique (CEA), DSM/DAPNIA, Centre d'Etudes de Saclay,
91191 Gif-sur-Yvette, France

[ck] Insitute of Physics, Academia Sinica,
TW-Taipei 11529, Taiwan and
Shandong University, School of Physics,
Jinan, Shandong 250100, P. R. China

[cl] University of Sheffield, Department of Physics & Astronomy,
Hounseld Road, Sheffield S3 7RH, U.K.

[cm] Insitute of Physics, Academia Sinica,
TW-Taipei 11529, Taiwan

[cn] SLAC National Accelerator Laboratory, Stanford,
California 94309, U.S.A.

[co] University of South Carolina,
Columbia, U.S.A.

[cp] Stockholm University, Department of Physics and The Oskar Klein Centre,
SE-106 91 Stockholm, Sweden

[cq] Department of Physics and Astronomy,
Stony Brook, NY 11794-3800, U.S.A.

[cr] Institute of Physics, Academia Sinica,
TW-Taipei 11529, Taiwan and
Sun Yat-sen University, School of physics and engineering,
Guangzhou 510275, P. R. China

[cs] Tbilisi State University, High Energy Physics Institute,
University St. 9, GE-380086 Tbilisi, Georgia

[ct] University of Toronto, Department of Physics,
60 Saint George Street, Toronto M5S 1A7, Ontario, Canada

[cu] University of Tsukuba, Institute of Pure and Applied Sciences,
1-1-1 Tennoudai, Tsukuba-shi, JP-Ibaraki 305-8571, Japan

[cv] University of California, Department of Physics & Astronomy,
Irvine, CA 92697-4575, U.S.A.

[cw] University College London, Department of Physics and Astronomy,
Gower Street, London WC1E 6BT, U.K.

[cx] University of California Santa Cruz, Santa Cruz Institute for Particle Physics (SCIPP),
Santa Cruz, CA 95064, U.S.A.

^{cy}*University of Illinois, Department of Physics,*
  1110 West Green Street, Urbana, Illinois 61801 U.S.A.

^{cz}*Instituto de Física Corpuscular (IFIC), Centro Mixto UVEG-CSIC,*
  Apdo. 22085, ES-46071 Valencia, Spain and
  Dept. Física At., Mol. y Nuclear, Univ. of Valencia, Valencia Spain and
  Instituto de Microelectrónica de Barcelona (IMB-CNM-CSIC),
  08193 Bellaterra, Barcelona, Spain

^{da}*University of Victoria, Department of Physics and Astronomy,*
  P.O. Box 3055, Victoria B.C., V8W 3P6, Canada

^{db}*University of Wisconsin, Department of Physics,*
  1150 University Avenue, WI 53706 Madison, Wisconsin, U.S.A.

^{dc}*Bergische Universitaet, Fachbereich C, Physik,*
  Postfach 100127, Gauss-Strasse 20, DE-42097 Wuppertal, Germany

^{dd}*Yale University, Department of Physics,*
  PO Box 208121, New Haven, CT06520-8121, U.S.A.

^{de}*Yerevan Physics Institute,*
  Alikhanian Brothers Street 2, AM-375036 Yrevan, Armenia

  E-mail: stathes.paganis@cern.ch

ABSTRACT: The reconstruction of photons in the ATLAS detector is studied with data taken during the 2004 Combined Test Beam, where a full slice of the ATLAS detector was exposed to beams of particles of known energy at the CERN SPS. The results presented show significant differences in the longitudinal development of the electromagnetic shower between converted and unconverted photons as well as in the total measured energy. The potential to use the reconstructed converted photons as a means to precisely map the material of the tracker in front of the electromagnetic calorimeter is also considered. All results obtained are compared with a detailed Monte-Carlo simulation of the test-beam setup which is based on the same simulation and reconstruction tools as those used for the ATLAS detector itself.

Contents

1 Introduction

In 2004 the ATLAS collaboration embarked on a Combined Test Beam (CTB) campaign, where a full slice of the barrel detector was exposed to particle beams (electrons, pions, muons, protons and photons) of energy ranging from 1 to 350 GeV. The main goals of this campaign were to study the detector performance in a controlled environment, to validate the description of the data by the Monte-Carlo (MC) simulation and to perform combined studies in a setup close to that of ATLAS (e.g. studies using the inner tracker with electromagnetic and hadronic calorimetry). One of these combined studies focuses on photon reconstruction. In the specific beam setup used for this study, photons were produced via Bremsstrahlung from 180 GeV electrons incident on a thin target upstream of the experimental apparatus. The goal of these runs was to study the reconstruction of converted and unconverted photons with and without magnetic field.

In ATLAS the photon energy is measured with the Liquid Argon (LAr) electromagnetic calorimeter [1]. The significant amount of material upstream of the LAr calorimeter (due to the tracker, services, cryostat etc., amounting to an average of $\sim 4X_0$ in the pseudorapidity range $-2.5 < \eta < 2.5$) necessitates a photon energy calibration which is different from the electron calibration in ATLAS [2]. This particle specific calibration is currently based on MC relying on the best knowledge of the amount of material upstream of the calorimeter. Photon calibration is a challenging task given that converted photons require different calibration from unconverted ones. Converted photons are those which convert in or upstream of the TRT tracker, while unconverted photons are those which arrive at the LAr cryostat without creating an e^+e^- pair. The identification of conversions by means of the inner tracker becomes thus a necessary step in the photon calibration. Both the reconstruction of converted photons and a careful calibration of the calorimeter response for photons are of great importance for physics measurements involving photons in their final state, e.g. the decay of the Higgs boson into two photons.

Several aspects of the photon beam analysis are presented in this note. By exploiting the full inner detector capabilities combined with the LAr calorimeter, the study of the reconstruction of photon conversions is performed. In addition, the difference in the reconstructed energy using the LAr calorimeter for e^+e^- pairs (from converted photons) and unconverted photons of the same energy is investigated. Finally the use of the converted photons for an estimation of the amount of the material in the different pixel layers is studied.

The detector layout is described in section 2, whereas the simulation of the experimental setup is discussed in section 3. Section 4 deals with the global event reconstruction and selection for further analysis. The reconstruction of converted photons contained in the same LAr cluster and unconverted photons, is presented in section 5. A detailed comparison of the response of the calorimeter to converted and unconverted photons is given, together with the systematic uncertainties of the analysis. The converted photon reconstruction is presented in section 6 and its application to evaluating the amount of material in the tracker in section 7 together with a study of the corresponding systematic uncertainties .

2 Experimental setup

2.1 The H8 SPS beam line

The H8 beam line in the North Area of CERN provides secondary and tertiary beams of hadrons, electrons or muons with energies from 1 to 350 GeV for the ATLAS test beam [3]. For this test beam, the secondary beam is produced by a proton beam with energies up to 400 GeV, extracted from the Super Proton Synchrotron. The protons impinge on the primary target (T4) producing showers of secondary particles from which the secondary beams are extracted. The creation of tertiary beams is handled by placing a second target 130m downstream of the primary target.

The H8 beam line consists of a number of quadrupole and dipole magnets, for focusing and bending the particle trajectories, and for defining the particle momentum by controlling the magnet currents. A large spectrometer constructed of six standard dipole magnets is used for the momentum definition.

2.2 The CTB reference system

The reference system is defined to be as consistent as possible with the ATLAS reference system. The (x, y, z) coordinates are defined as follows:

- x-axis along the H8-beam;

- y-axis vertically upwards;

- z-axis horizontally;

- $x = y = z = 0$ on the nominal axis of the H8-beam, at the front surface of the CTB magnet used to emulate the ATLAS solenoidal magnetic field (MBPS).

The CTB magnet is a dipole providing a magnetic field of 1.4 Tesla over a length of 1.5 m resulting in the deflection of positively charged particles along positive y. Therefore, the y and z measurements in the CTB setup correspond to the ϕ and η measurements in ATLAS.

2.3 Photon beam line

As illustrated in figure 1, the secondary 180 GeV positron beam impinges on the Pb target at x = −27500 mm, where in turn Bremsstrahlung photons are emitted. Downstream, there are two-magnet systems MBPL12 (1.5 T) and MBPL13 (1.35 T), located at x = −11702 mm and x = −15500 mm respectively. The magnets are used to separate the primary positron from the radiated photon. The first magnet separates the positron from the photon in the z direction, while the second one deflects it in the y direction. The separation changes by applying different magnetic fields. Each magnet has a maximum bending power of 3.8 Tm. Positrons are triggered by a small scintillator (8x8 mm^2), placed at x = −1675 mm, which determines therefore the position, i.e. the momentum, of the outgoing positron. This has a mean value of about 120 GeV with a 10 GeV spread coming from the spread of the incident positron position and the width of the scintillator. Given that both positrons and photons lose energy as they traverse material - 0.66 X_0 and 0.51 X_0 respectively - before hitting the LAr Calorimeter, it is essential to accurately account for the total amount of material along the beam line (see table 1).

Table 1. Breakdown of the amount of material in the H8 beam line for the photon setup.

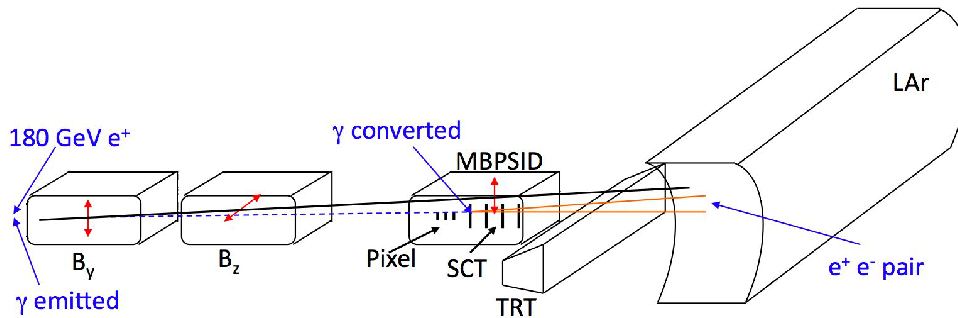|	Positrons	Photons
In front of the Pb target	15% X_0	—
From the Pb target to the front face of the CTB magnet	13% X_0	13% X_0
From the front face of the CTB magnet to the exit of the CTB magnet	25% X_0	25% X_0
From the exit of the CTB magnet to the cryostat	13% X_0	13% X_0
Total	66% X_0	51% X_0

Figure 1. Schematic view of the photon beam setup.

The photon runs can be divided into two main categories depending on whether the B-field is on or not. In the second case the silicon trackers have been removed from the beam line. In this paper results from runs with the B-field on are presented, while the B-field off runs are used for studying various systematic effects.

2.4   The detectors

The entire volume of the test beam setup (see figure 3) has been designed to include all sub-detectors in addition to the pre-existing beam line elements. Exact coordinates for each sub-detector can be found in [4]. The relevant detectors for the measurements presented in this paper are the tracker, which consists of three sub-systems, the pixel, the silicon strips tracker (SCT) and the transition radiation tracker (TRT) (see figure 2), and the calorimeter.

The pixel detector consists of three layers (Pixel B, Pixel 1 and 2). Each layer has two modules, and each module has an active size of $z \times y = 60.8 \times 16.4$ mm^2. Each module is positioned at an angle of 20° and with superposition of the two modules in Layer 1 and 2 of 0.2 mm. For the photon runs, a thin copper foil was placed at a distance of 77 mm upstream from the front of the pixel box. It is 37 μm in thickness corresponding to 0.25 X_0 in radiation lengths with transverse dimensions of 55×105 mm. It provides a reference point for the material measurement described in section 7.

The SCT detector consists of 4 layers with 2 modules per layer, each module covering an area $z \times y = 120 \times 60$ mm^2. There is a 4 mm overlap between the upper and lower modules in the layer. The two middle modules are centered vertically with respect to the beam axis, while the first and
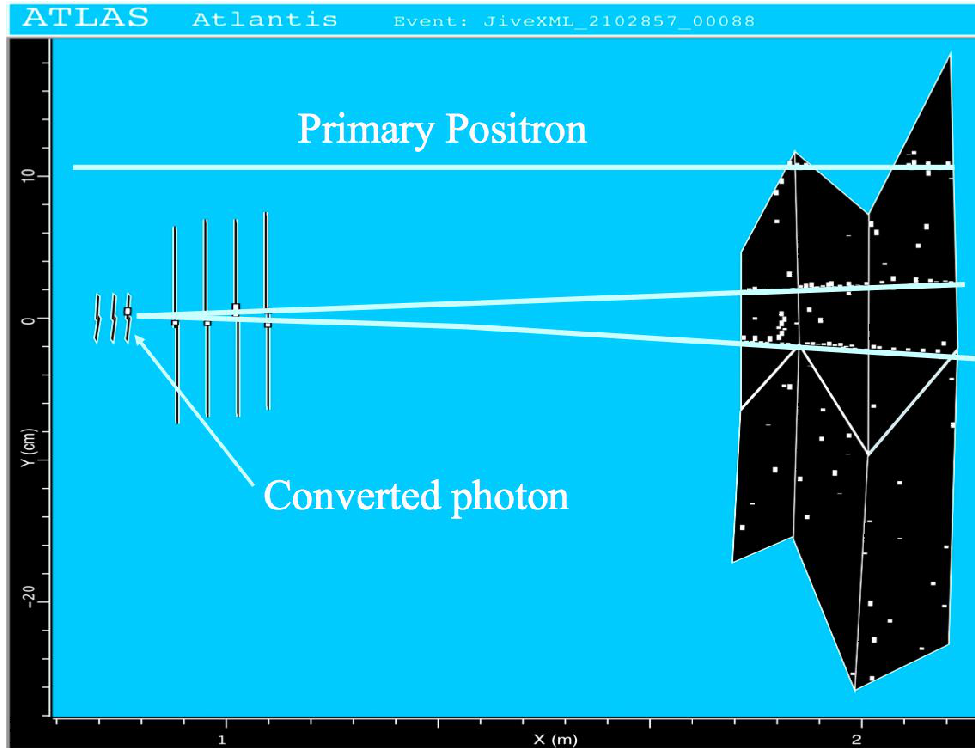
– 4 –

Figure 2. Event display of a converted photon as seen in the CTB setup. The three tracker sub-systems are visualized. Starting from the left these are the pixel, the silicon strips and the transition radiation tracker. See text for a more detailed description of each one of them.

last ones are offset in y by -5 mm and $+5$ mm respectively. Everything is enclosed within a box of dx $=$ 330 mm, dy $=$ 300 mm and dz $=$ 200 mm, and the box starts from x $=$ 347 mm. The front silicon side of the lower module in the third SCT layer was not operational.

The TRT detector is made of two barrel wedges. Each barrel wedge is equivalent to $1/16$ of the circumference of a cylinder, with inner radius of 558 mm and outer radius of 1080 mm and overall length of 1425.5 mm. The center of the cylindrical wedge is located at x $=$ 1152 mm, z $=$ 550 mm, while its y position is located at -8 mm for the photon runs. Its angular extent, including the support structures, is $\Delta\phi = 28.125°$, starting at $\phi = -17.375°$. One TRT barrel wedge consists of three modules.

The distance in ATLAS between the last SCT layer and the first TRT plane is 40 mm, while in the Combined Test Beam layout it is increased to ≈ 1114 mm, leaving a clearance of about 345 mm between the magnet coils and the TRT support structure.

Both the SCT and pixel modules are placed inside a permanent dipole magnet called the MBPS magnet that generates the magnetic field necessary for the track reconstruction. Due to space considerations, the TRT module is kept outside.

The calorimeter is positioned after the TRT sub-detector. Module 0 of the Liquid Argon (LAr) electromagnetic barrel calorimeter is placed inside a cryostat. Due to the large size and shape of the

Table 2. Granularity of Module 0 of the liquid argon calorimeter in the barrel region.

	Cell size in units of η	Cell size in units of ϕ
Presampler	0.025	0.1
Strips	0.0031	0.098
Middle	0.025	0.0245
Back	0.05	0.0245
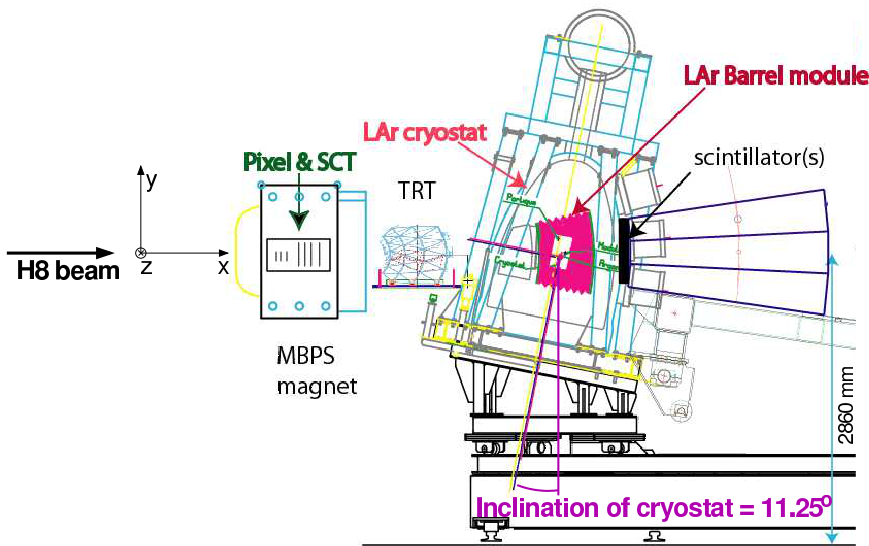
Figure 3. Schematic of the test beam setup. The beam particles first hit the pixel and SCT modules and then continue towards the TRT, calorimeters and muon modules.

cryostat, an argon excluder (a block of Rohacell[1]) was installed in front of the module to minimize the amount of passive material just in front of the EM calorimeter. Its total thickness is greater than 22 radiation lengths (X_0) in the barrel. The calorimeter, being of accordion shape, is segmented into three longitudinal sections called layers ("front" or "strips", "middle" and "back"). The calorimeter is preceded by a presampler device. The granularity of the calorimeter and presampler (cell size) is described in table 2 [2].

Behind the back wall of the cryostat, three hadronic calorimeter modules are stacked. These are iron scintillating tile sampling calorimeters. All calorimeter modules (82 tons) are placed perpendicular to the beam line and are supported on a rotating table. The table rotates about the vertical axis and translates along the z (horizontal) axis. These two motions allow for the simulation of different impact points in η. The table, however, cannot be rotated in ϕ, therefore, to simulate different impact points in ϕ a deflecting magnetic field is needed.

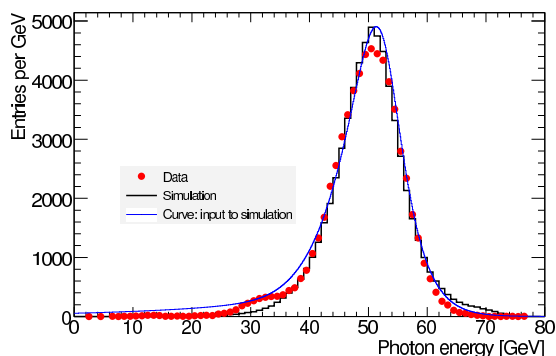[1]Rohacell is a rigid-foam with very low density.

Figure 4. Measured energy spectrum for triggered unconverted photons (full circles). Also shown are the functional form used as an input to the simulation for the photon energy spectrum (curve) and the resulting reconstructed energy spectrum for the simulation (histogram).

3 Monte Carlo simulation of the test beam setup

One of the most challenging aspects of the analysis reported here, is the Monte Carlo simulation of the photon run. This section describes the necessary steps for the production of the Monte Carlo samples using the ATLAS software framework for the photon runs, as well as the needed corrections applied to the Monte Carlo in order to obtain as close as possible a description of the data.

3.1 Particle generation

At the particle generator level, one can determine the type of particle to be generated, its energy, the calorimeter coordinates, the beam spot as well as the starting point of the beam. The particles, are then sent to Geant4 [5] for a complete detector simulation. Geant4 uses Monte Carlo methods to simulate the physics processes when particles pass through matter. For a detailed description of the CTB experimental setup in Geant4 see [6].

In the case of the photon runs, the photon beam is created from an original positron beam with nominal energy of 180 GeV. This results to two correlated particles (a positron and a photon) being present, whose momentum spectra are not monochromatic and which for each event add up to the nominal original beam energy. Therefore, to properly simulate this configuration, the particle generator is modified in order to be able to handle two particles with known energy spectra. The photon spectrum is derived from the data using triggered unconverted photons and reconstructing the cluster energy as described in [4] without any corrections applied. This spectrum is then parametrized and its functional form is fed into the particle generator. During successive iterations the input photon spectrum to the particle generator is adjusted so that the agreement of the reconstructed photon spectrum between the data and the simulation is good. In figure 4 such a measured photon spectrum is shown. Also shown is the functional form used as an input to the particle generator and the resulting reconstructed energy spectrum after the simulation. The small bump present in the data at ~ 30 GeV is due to secondary photons due to bremsstrahlung losses of the primary high energy positron upstream of the tracker. Finally the corresponding positron energy is determined by subtracting the photon energy from the original positron beam nominal energy.

Table 3. Monte Carlo parameters for the photon test-beam event generation

Category	e^+	γ
Total Energy (GeV)	179.2 - E$_\gamma$	Taken from data shown in figure 4
Generation Point x [mm]	-27500	-1100
y [mm]	9.7 - 19.7	mean= 1.07, σ=3.5
z [mm]	44.6 - 54.6	mean= 27.0, σ=2.94
ϕ angle [rad]	-	mean= -0.0017, σ=0.0002
θ angle [rad]	-	1.568

3.2 Beam conditions

To ensure optimal agreement between the simulation and the collected data, the beam conditions, such as the profile and the divergence of the produced photon beam, need to be properly estimated. This is done by using the track parameters at the *perigee* of the converted photons reconstructed in the silicon tracker. The *perigee* is a reference point located at the entrance of the bending magnet enveloping the silicon tracker (MBPS). Since the photon beam conditions using converted photons can only be derived from the data at a location right in front of the MBPS magnet, the origin of the photon beam in the simulation is placed 1.1 m in front of it. All the upstream material that the photons should have traversed up to this point,is then condensed into an aluminum block with an equivalent thickness of 13% of a radiation length positioned 1 m in front of the MBPS magnet. The original positrons on the other hand are created much earlier at -27.5 m allowing them to pass through the upstream bending magnets and deflected away from the photon beam. The simulation of the beam profiles of both the original positrons and the photons ensures that the two beams traverse the CTB line and impact the electromagnetic calorimeter realistically reproducing the data behavior. The parameters used by the simulation for the runs with the MBPS magnet enveloping the silicon tracker turned on, are listed in table 3.

3.3 Digitization

The output of the Geant4 simulation needs to be digitized before it can be reconstructed. Digitization is a process whereby the output of the detector simulation called *hits* is converted to a raw-data format. This stage emulates the effects of the readout chain such as electronic noise and cross-talk. The file obtained during the digitization can then be processed by the reconstruction software.

4 Event reconstruction and selection

In this section a summary of the inner tracker and LAr calorimeter reconstruction algorithms relevant to the photon reconstruction is presented.

4.1 Data sample

For the work presented in this paper, only runs with an incoming photon beam and with magnetic field on are presented. For these runs the silicon tracker is present in the beam line and the magnetic field is at its nominal value. They amount to $\sim$300000 events.

4.2 Track reconstruction

In order to properly identify photon conversions a dedicated track reconstruction sequence has been implemented and adapted to the specific geometry of the CTB setup. The standard tracking method used is the so-called *Inside − Out* tracking. The name stems from the fact that the track reconstruction starts from the silicon tracker and progresses towards the TRT tracker. First a silicon track segment is reconstructed starting from the largest number of silicon (both pixel and SCT) hits that fall into a line (straight line when the magnetic field is off, a circle when on). Fast fits are performed to determine which of these hits will be retained starting from the first three silicon hits and then gradually adding more. This substantially reduces the combinatorics without any loss in efficiency. As soon as the silicon track segment has been formed in this manner, TRT extensions are added to it assuming that the track stays within the fiducial acceptance of the TRT detector. The final track parameters are then determined by a global χ^2 minimization of the residuals (defined as the difference between the measurement position and the one predicted by the track) and their errors. For more details see [7]. The *Inside − Out* tracking is very efficient in reconstructing tracks in particularly busy environments since the high granularity of the silicon trackers can provide the necessary resolution for recovering the track-hit pattern. However, this algorithm is limited to reconstructing tracks that originate in the pixels or the first SCT layer, since a minimum of seven silicon hits are required for a track in order to be reconstructed.

To remedy for this, a complementary algorithm aiming at reconstructing primarily tracks from secondary particles, such as those originating from photon conversions, is also used. This will be referred to as the *Back*-tracking algorithm. Here track segments are first reconstructed inside the TRT tracker. The reconstructed TRT track segments are then extrapolated backwards towards the silicon tracker. Silicon space-point seeds are then searched for in the three SCT layers closest to the TRT. A minimum of two space-points is required in this case. After the space-point seed formation additional hits are then added layer-by-layer and the track parameters are computed using the Kalman-filter formalism [8]. The track parameters are updated after every successive hit has been added and outliers are immediately eliminated through their large contribution to the χ^2 of the track fit. For more details on the *Back*-tracking reconstruction algorithm and on how the tracks are used afterwards for the reconstruction of photon conversions in the ATLAS tracker, see [9].

Finally, the tracks reconstructed by the two algorithms are combined and any overlap between the resulting track collections is removed as explained in more detail in section 6.1. This then constitutes the final track collection to be used for reconstructing photon conversions inside the tracker.

4.3 Cluster reconstruction in the LAr calorimeter

A cluster in the LAr calorimeter is formed by a group of cells. A simple projective cone algorithm is used to collect the cell energies in clusters (see [4] and references therein). Starting from cells in the middle layer, the most energetic cell is taken as the seed of the cluster and a fixed window $\Delta\eta \times \Delta\phi = 0.075 \times 0.125$ (corresponding to 3×5 middle cells) is built around the seed. The choice of the cluster size is a compromise between electronic noise and shower energy containment. The size along η is consistent with the Moliere radius of an EM shower in the calorimeter, while the larger size along ϕ is chosen in order to contain the conversion electrons separated by no more than half a cell while entering the calorimeter. A geometrical projection is then made to the other layers

of the calorimeter. The total cluster energy is obtained from the sum of the energy deposits in each layer of the cluster. For the analysis reported here, no cluster energy corrections were applied in contrast to [4] and [10].

4.4 Event selection

After the reconstruction of tracks and clusters, events can then be selected by exploiting their characteristics. The selected events fall into two complementary categories according to the aim of the final analysis. The first category includes events with two well separated clusters of size $\eta \times \phi$ = 3×5 in the LAr calorimeter. One cluster corresponds to the photon with an approximate energy of 60 GeV (converted or unconverted) and the other to the primary positron with energy $\simeq$ 120 GeV. The second category involves events with 3 clusters corresponding to the well separated e^+e^- conversion pair and the high energy positron. Further event selection involves examining the characteristics of the reconstructed TRT track segments. Those produced by electrons from photon conversions tend to cluster closer to the central region along the vertical direction of the TRT volume. In contrast to conversions, the original positron having been deflected upwards in order to avoid the silicon tracker, will reach the TRT detector at a much higher position. TRT track segments that point towards the center of the silicon tracker when extrapolated backwards, should therefore belong to converted photons, whereas the ones pointing higher missing the silicon tracker altogether, should be due to the original positron. Figure 5 shows the distributions of the vertical y-positions after a straight line extrapolation to the center of curvature of the TRT barrel wedge of the observed TRT track segments located downstream of the last silicon tracker layer outside the MBPSID magnet. The charge can be defined by looking at the segment slopes during the extrapolation and the positively charged tracks are plotted separately in the same figure. As expected, the TRT track segments due to the original positron are indeed characterized by higher vertical displacements. Events for both analysis categories can therefore be selected by requiring the tracks from the photon conversions to be closer to the TRT central vertical region as figure 5 suggests. The larger separation of the converted photon tracks in the simulation plot (left) as compared to that in the data is largely due to the TRT detector misplacement along the beam line (x-axis) with respect to the silicon sub-systems in the tracker. This is primarily due to the fact that the TRT was outside the tracker magnetic field making it thus difficult to identify shifts along the beam axis. The larger number of tracks on the data side characterized by large positive displacements from the TRT central vertical region as compared to the simulation, is due to the fact that the original positron traverses in reality a larger amount of material upstream of the tracker than that introduced in the simulation. This results in larger track activity, due for example to secondary tracks from electromagnetic showers. This discrepancy does not in any way affect the converted photon analysis presented in section 6. To ensure an even cleaner photon sample selection, an additional requirement is that there be no tracks outside the central TRT region. These stringent selection criteria do not exclude the possibility of very asymmetric conversions where the electron/positron with the lower energy is swept out of the TRT detector acceptance. From simulation studies it is expected that these events account for less than 0.4% in the overall selected sample; thus rendering their impact negligible.

The events in the first category are used for the the measurement of the small difference in the calorimeter response expected between converted and unconverted photon energy depositions. This procedure is described in detail in section 5. The events in the second category are used to study
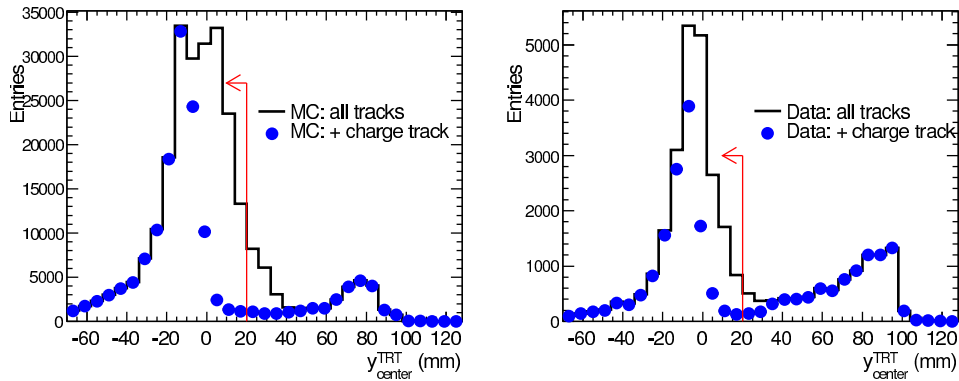
Figure 5. Extrapolated y-position of the TRT track segments at the center of the TRT barrel wedge for simulated (left) and real data (right). TRT track segments due to the original positron are clearly characterized by higher vertical displacements.

the reconstruction of converted photons in the first tracker layers (pixels) with the main goal of estimating the amount of material in front of the calorimeter. This is presented in detail in section 6.

5 Comparison of calorimeter response for converted and unconverted photons

The main goal of the analysis presented in this section is to study the differences of the calorimetric response to photons that have not converted inside or before the TRT, to photons that have converted. Differences are expected in the presampler and the three layers of the calorimeter due to the early commencement of the shower in the case of a conversion. In addition, the total energy (the sum of the energy in the four LAr compartments) is also expected to exhibit a difference. This difference is not only due to the additional energy loss in the upstream material in the case of a conversion, but also due to the drop of the effective sampling fraction in the calorimeter as a result of the early showering [10].

These variations in calorimetric response between converted and unconverted photons reported here, and their subsequent agreement with MC, support the use of distinct calibrations for electrons and photons applied in ATLAS.

5.1 Single photon cluster selection

In this work results from photon runs in the first category with two clusters and B-field on are presented. These runs provide a particular topology for most events as can be seen in the schematic of figure 6. In order to proceed with the study, events with the separation shown in figure 6 are selected. The selection criteria imposed in this work are described in table 4.

5.2 Calorimeter response to photons contained within a single cluster

The presence of material upstream of the LAr calorimeter complicates the photon reconstruction since a 25% of the photons convert before reaching the cryostat. The CTB provides us with the opportunity to study the response of the LAr calorimeter with the presence of magnetic field in the

Table 4. Selection criteria for Data and MC for photon runs with the magnetic field on.

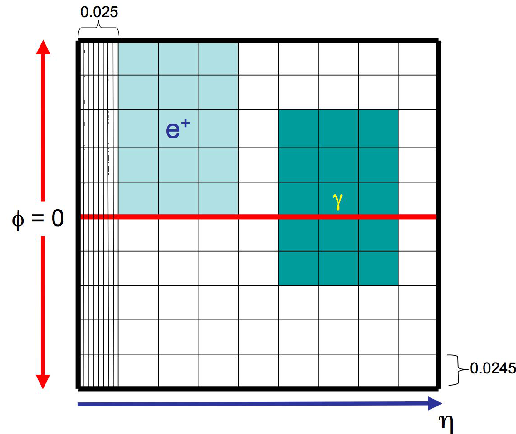| Run	B≠0	
	Photon	Positron
Cluster-η	$0.538 < \eta < 0.542$	$0.455 < \eta < 0.46$
Cluster-ϕ	$0.001 < \phi < 0.01$	$0.07 < \phi < 0.085$
No. of cells	79	79

Figure 6. Expected topology in the $(\eta \times \phi)$ plane of energy deposits from the beam positron and the radiated photon in the middle layer of the EM Calorimeter.

silicon tracker region. For the final analysis the separation between converted and unconverted photons is performed using the TRT. For the identification of converted photons the following selection is applied:

- At least one TRT track in the photon path.

- One TRT track in the primary positron path or number of high level (HL) charge threshold hits in the TRT greater than zero. This cut is necessary in order to 'tag' the positron.

- No TRT tracks outside the photon/positron paths.

For the identification of unconverted photons the following selection is applied:

- No TRT tracks in the photon path.

- No HL hits in the photon path.

- At least one TRT track in the primary positron path or number of HL hits greater than zero.

The efficiency of the TRT-based selection was confirmed by performing a simulation and comparing the calorimetric distributions of true converted and unconverted photons with the corresponding
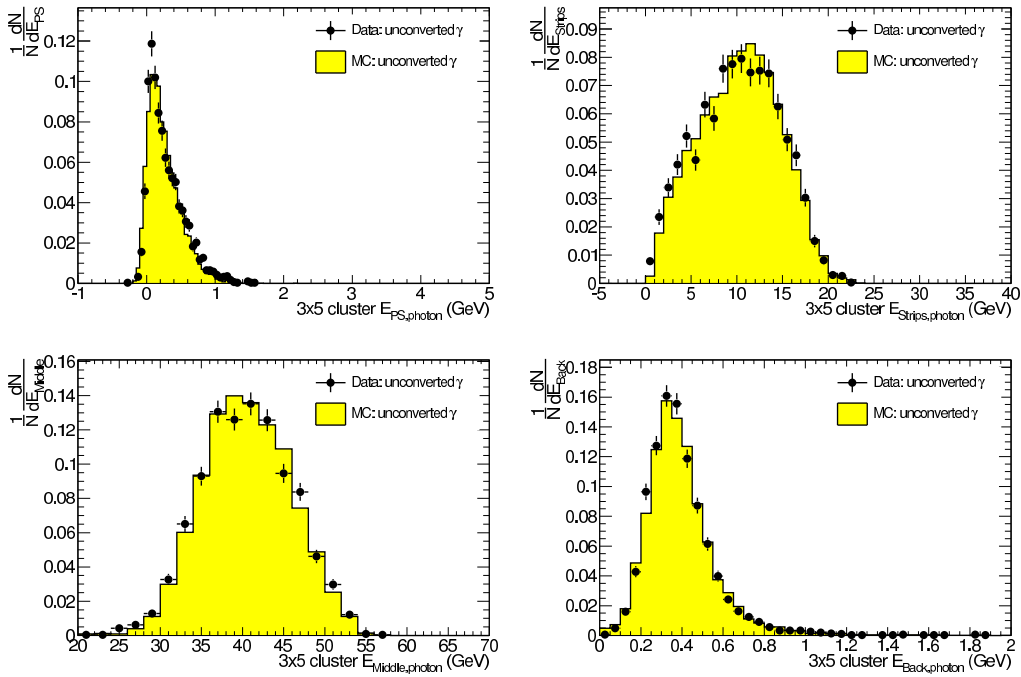
Figure 7. Total energy deposited in each compartment of the calorimeter for data and Monte Carlo for unconverted photons for a run with the magnetic field on.

distributions obtained when the TRT was used for the tagging. The comparison showed that the TRT can separate the two photon populations very efficiently (99.5% of the converted photons are tagged by the TRT) thus effectively removing any systematic effect coming from the TRT tagging.

Figures 7 and 8 show the four layer energy distributions for data (bullets) and MC (histograms) for unconverted and converted photons respectively. The observed agreement between the data and the Monte-Carlo for both samples indicates an accurate description of the material by the simulation.

Figure 9 compares directly for the data the layer energy distributions for converted and unconverted photons. A clear discrimination in the longitudinal shower development is observed: photons which convert before the beginning of the TRT develop an earlier shower, thus depositing more energy in the presampler and strip layer of the calorimeter.

In figure 10 the sum of the energies of the four layers of the positron and photon clusters (i.e. the total cluster energy) is presented for converted and unconverted photons. Given that the positrons remain unaffected by the conversion/no-conversion separation, the shift in the energy measured in the calorimeter can be seen either in the photon total energy distribution or in the total combined photon and positron energy (see figure 10).

The differences between converted and unconverted photons in the total cluster energy, defined here as the sum of the raw energies of all cells in the cluster, can be expressed in terms of a
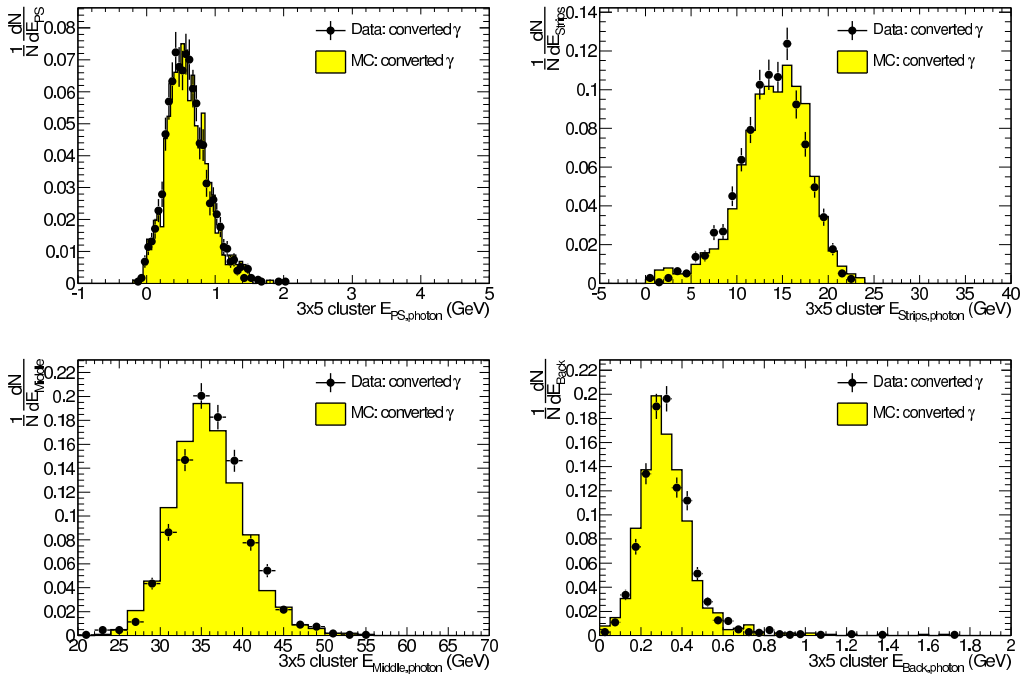
Figure 8. Total energy deposited in each compartment of the calorimeter for data and Monte Carlo for converted photons for a run with the magnetic field on.

Table 5. Photon energy scale shift measurement obtained from the total positron-photon energy, and the photon energy alone, for runs with the magnetic field on.

| Method | **R**: fractional energy shift for converted vs unconverted photons | |
	Data	MC
B≠0, E_γ+E_{e^+}	1.45±0.14 (stat) ± 0.15 (sys) %	1.54±0.09 (stat) %
B≠0, E_γ	1.16±0.22 (stat) ± 0.15 (sys) %	1.39±0.26 (stat) %

fractional difference **R** as follows:

$$\mathbf{R} = \frac{E_{\text{Tot,Unconverted}\gamma} - E_{\text{Tot,Converted}\gamma}}{E_{\text{Unconverted}\gamma}}. \tag{5.1}$$

The ratio **R** is a useful measure of how well the MC describes the data. This is shown in table 5 using two methods. The first method uses the sum of the energy of the two clusters for the two types of events, and attributes the measured energy difference to the energy difference between converted and uncoverted photons. The second method uses only the energy of the photon cluster. A problem with the latter is that although the initial beam energy is fixed, the photon cluster energy is not monochromatic leading to difficulties in the fitting procedure. This is reflected in the larger statistical uncertainty systematic, dominated by uncertainties in the fit. In the data a fractional shift of 1–1.5% is observed consistent with the prediction of the MC simulation.
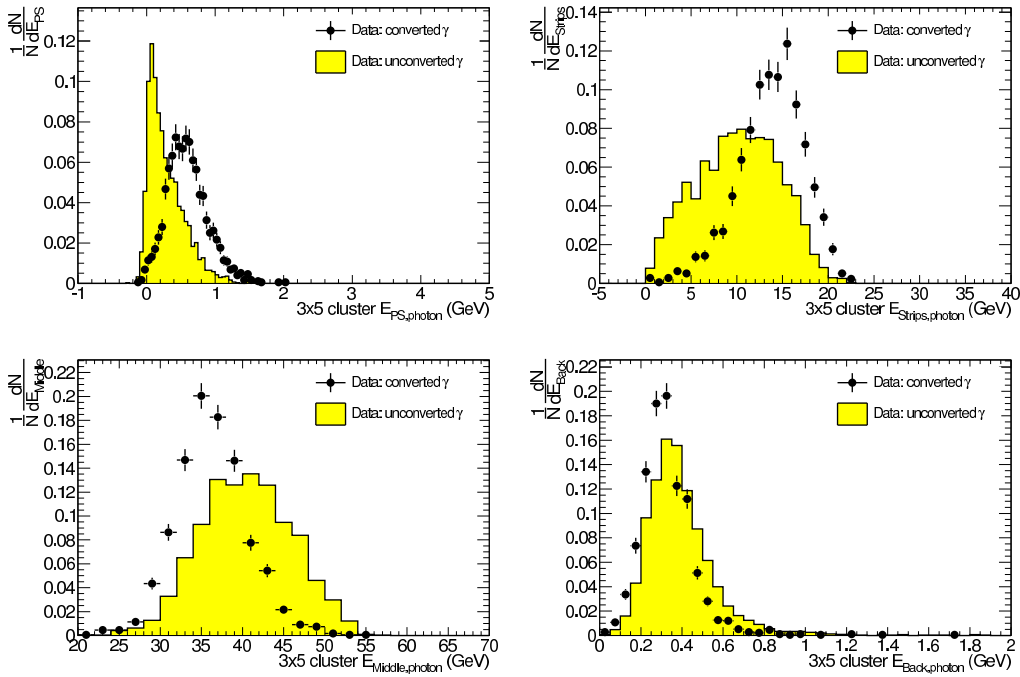
– 14 –

Figure 9. Energy distributions in the four layers of the calorimeter for a data run with the magnetic field on. The separation between converted (bullets) and unconverted (histogram) photons using the TRT is shown. A clear discrimination in the longitudinal shower development is observed: photons which convert up to the TRT develop an earlier shower, thus depositing more energy in the presampler and first sampling of the calorimeter, and less energy in the middle and back samplings.

5.3 Systematic uncertainties on the fractional energy difference

A comprehensive list of the systematic uncertainties is given below along with their calculation method and their values. Variations of analysis cuts and correction factors have been applied in order to get an estimate of the uncertainties. Their effect on the energy scale difference has also been computed and tabulated. The effect of uncertainties in the amount of material upstream of the calorimeter has also been studied. The most important sources of systematic uncertainties are:

- Beam absolute energy scale: The nominal positron beam energy in the region of 180 GeV has an uncertainty of 0.5-0.7% [4]. To test possible systematic effects of this uncertainty the incident positron energy scale was varied by $\pm 1\%$. The overall effect on the ratio **R** is less than 0.05% since this uncertainty affects both samples in the same way.

- Presampler uncertainty (MC only): Uncertainties in the knowledge of the absolute energy response in the presampler are of order 6% and may also affect the ratio **R**. A conservative 10% variation of the presampler energy response in the MC results in a 0.1% uncertainty on the ratio **R**.

- Cross-talk effects in the LAr calorimeter: They are measured by pulsing cells and measuring the induced signal to neighboring cells. Corrections to the responses of the cells are then
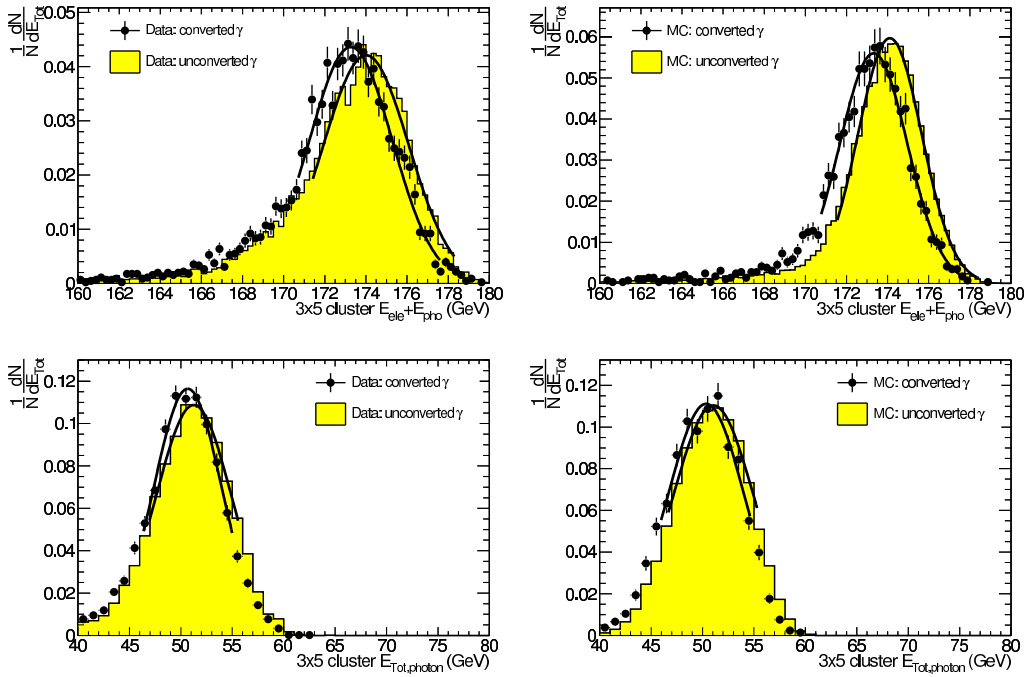
Figure 10. Top: the combined positron and photon cluster energy distribution for converted (bullets) and unconverted (histogram) photons for Data (left graph) and MC (right graph) for a magnetic field on run. The obtained difference in the photon cluster energy before calibration is $1.45 \pm 0.14\%$ for data and $1.54 \pm 0.09\%$ for MC. Bottom: photon energy distribution for converted (bullets) and unconverted (histogram) photons for Data (left graph) and MC (right graph) for a magnetic field on run. The obtained difference is $1.16 \pm 0.22\%$ for data and $1.39 \pm 0.26\%$ for MC consistent with the total energy fractional shifts.

implemented in the MC simulation. The impact of such cross-talk effects to the ratio **R** can be studied by varying the level of cross-talk in the simulation. The largest effects are due to uncertainties in the inter-strip cross-talk correction which can lead to variations of 1% in the strip layer energy response. The induced systematic uncertainty on the ratio **R** is less than 0.04%.

- Upstream material: Uncertainties in the knowledge of the amount of material upstream of the CTB experimental setup may also impact the ratio **R**. This was studied by running the full analysis after varying the amount of material upstream, from 0 to 20% X_0. Even such large a variation did not produce a significant change on the ratio **R**.

Table 6 summarizes the systematic uncertainties on the fractional shift **R** of the cluster energy for converted photons. The total systematic uncertainty is no more than 0.15%.

In summary, the obtained values of the ratio **R** are in good agreement with MC expectations. The fact that **R**$\neq$0 is the main reason for providing specific calibrations for electrons, unconverted and converted photons within the ATLAS electron-photon reconstruction software.

Table 6. Systematic uncertainties in the fractional energy shift **R**.

Effect Name	Systematic Uncertainty in **R**	Variation Applied
Beam Energy Scale	±0.05%	+1% -1%
Presampler Uncertainty	±0.10%	+10% -10%
Strips	±0.04%	+1% -1%
Extra Material Upstream of Magnets	±0.005%	
TOTAL	±0.15%	

6 Reconstruction of converted photon vertices

A large fraction of the beam photons will convert as they traverse the silicon tracker. The two tracks from the emitted e^+e^- pair can then be used to reconstruct the conversion vertices. For the studies presented in this section only photons that convert in the pixel tracker will be considered. This allows for the produced tracks to have a sufficient number of precision silicon hits for their track parameters to be accurately computed. This in turn results in a much higher precision for the reconstructed vertex position. Since the number of converted photons is directly correlated to the amount of material inside the silicon tracker, they can be used for mapping the material of the pixel tracker. This procedure is described in the following section.

6.1 Tracks used in the photon conversion reconstruction

For reconstructing the converted photon vertices, all tracks delivered by the two tracking algorithms described in section 4.2 are used. In order to remove tracks reconstructed by both algorithms, tracks found by the *Back*-tracking algorithm are removed if they share more than 3 silicon hits with any of the tracks from the *Inside − Out* tracking algorithm.

About 80 % of the events have at least two tracks. Events with more than two tracks contain secondary conversions by Bremsstrahlung photons inside the silicon tracker. Events with less than two tracks contain photons that convert late inside the tracker, i.e. later than the second SCT layer (late conversions). The reconstruction of tracks from the late photon conversions is more challenging due to the reduced number of available precision hits and are not considered further here.

6.2 Converted photon event selection

Clean photon events are initially selected by requiring the total photon energy deposited in the LAr calorimeter to be

$$E \; > \; 42 \text{ GeV}, \tag{6.1}$$

where E is the total reconstructed photon energy in the LAr Calorimeter. In addition, events with unconverted and late converted photons are removed by requiring at least one reconstructed track in the TRT and one reconstructed space-point in the SCT.

$$N_{\text{sp}}^{\text{SCT}} > 0, \qquad (6.2)$$

$$N_{\text{track}}^{\text{TRT}} > 0, \qquad (6.3)$$

Events are further selected by examining the number of straw hits that the reconstructed TRT tracks in each event contain. A TRT track produced by an electron from a photon conversion contains, on average, 35 hits. On the other hand, the primary positron is steered by the bending magnets to almost miss the transition radiation tracker. As a result its TRT track segment will contain very few hits. In order to select TRT tracks originating from a photon converted inside the silicon tracker, the following condition is then applied:

$$N_{\text{hits}}^{\text{TRT}} > 27 \qquad (6.4)$$

Finally, events are also selected by examining the pointing of the TRT track segments when they are extrapolated backwards to the silicon tracker as discussed in section 4.4. In order to eliminate the TRT tracks due to the primary positron, those with positive charge should satisfy the following requirement:

$$\text{y}_{\text{center}}^{\text{TRT}} < 20 \text{ mm} \qquad (6.5)$$

where $\text{y}_{\text{center}}^{\text{TRT}}$ is the y position at the center of the TRT cylindrical wedge.

Table 7 shows the photon events classified according to the number of TRT tracks that pass the above selection criteria (designated as *good* TRT tracks) for both data and simulation. After pre-selection, 16 % and 17 % of the reconstructed simulation and data events remain, respectively. As it can be seen in this table, one or two TRT tracks are missing in about 37 % and 52 % of the simulation and data events, respectively. Events with no *good* TRT tracks correspond to those with unconverted photons or to those with converted photons that failed the directionality criterion in eq. 6.5. The significant discrepancy between the data and the simulation is due to the actual nature of the simulated photon beam. Although its energy spectrum and direction are derived from the data, they are based on converted photons that have essentially passed the above selection criteria, since these are the only photons that can be efficiently reconstructed. Stray photons, that may result in certain cases in electromagnetic shower bursts, have been omitted. As a result, the simulated photon beam is much cleaner than that in reality and hence the lower number of events with no *good* TRT tracks. The reverse is seen in the case of events that have two or more *good* TRT tracks, which account for 63 % and 48 % of the total simulation and data samples, respectively. This category includes conversion events from non-primary photons, i.e. Bremsstrahlung photons from the primary positron upstream of the MBPS magnet or secondary photon conversions from inside the tracker. As a result, two reconstructed *good* TRT tracks do not always match an e^+e^- pair from the primary photon conversion in the truth information. In the results presented below only events with two or more *good* TRT tracks are used.

Table 7. Comparison between Data and MC on number of events classified using *good* TRT tracks.

Sample	MC			Data
Processed events	839219			308867
After pre-selection	137557 (16 %)			53302 (17 %)
	MC	converted γ	matched to e^+e^-	Data
$N_{\mathrm{TRT}}^{good} = 0$	11002 (8 %)	886	—	11530 (22 %)
$N_{\mathrm{TRT}}^{good} = 1$	39537 (29 %)	30834	—	16148 (30 %)
$N_{\mathrm{TRT}}^{good} = 2$	76709 (56 %)	75703	73073	21712 (41 %)
$N_{\mathrm{TRT}}^{good} > 2$	10309 (7 %)	10069	8849	3912 (7 %)

6.2.1 Tracking efficiency and purity

The tracking efficiency and purity are estimated from the simulation by examining the reconstructed tracks that are assigned to converted photons inside the tracker. Both reconstructed tracks are required to correspond to a true e^+e^- pair that originates from the same true primary photon that converts inside the silicon tracker. The efficiency ($\mathscr{E}_{\mathrm{Trk}}$) to reconstruct the conversion tracks as well as the purity ($\mathscr{P}_{\mathrm{Trk}}$) of the reconstructed track sample as a function of the silicon tracker layers that they originate from, can be defined as,

$$\mathscr{E}_{\mathrm{Trk}}(i) = \frac{\text{Number of reconstructed tracks in layer } i}{2 \times \text{Number of conversions in layer } i}, \tag{6.6}$$

$$\mathscr{P}_{\mathrm{Trk}}(i) = \frac{\text{Number of true conversion-matched reconstructed tracks in layer } i}{\text{Number of reconstructed tracks in layer } i} \tag{6.7}$$

If an event has more than two reconstructed tracks, the number of reconstructed tracks is set to two.

Figure 11 shows the tracking efficiency in each silicon layer both for tracks reconstructed by the *Inside − Out* algorithm only and for the combined tracks. For early conversions occurring in the pixel layers, the efficiencies are ~ 90 % with the *Inside − Out* tracking method. On the other hand, as expected, they are lower in the case of late conversions due to the lack of sufficient number of hits to reconstruct those tracks using this method. In addition, given that the tracks from late conversions are very close to each other, only one track is usually observed for these events by the *Inside − Out* track reconstruction method. If both the *Inside − Out* and *Back*-tracking methods are applied, the tracking efficiency increases substantially for the late conversions. Figure 12 shows the purity when both tracking methods are used as a function of the position of the conversion vertex. The purity, except for the last layer of the SCT, is ~ 90 %. The degradation of the purity in the last SCT layer is mostly due to the increased presence of tracks from secondary (i.e. Bremsstrahlung) photon conversions.

6.3 Vertex reconstruction

In order to reconstruct photon conversion vertices the *VKalVrt* algorithm is used [11]. This is suitable for the reconstruction of any vertex type, be it primary or secondary. Based on the Kalman-
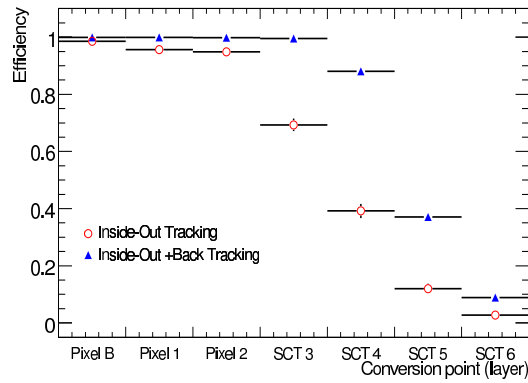
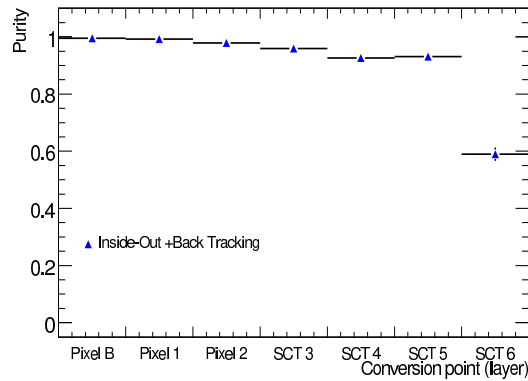**Figure 11**. Tracking efficiency in each silicon layer.

Figure 12. Purity of the reconstructed track sample in each silicon layer.

filter method, it allows the setting of many constraints such as mass and opening angle between the two tracks at the vertex. The input to the vertex fitter consists of a pair of tracks with opposite charge. For events with more than two tracks, the best combination is selected, determined by the distance of minimum approach of the two tracks.

For optimal results the $VKalVrt$ vertex fitter is called twice. First an initial vertex fit is performed without applying any constraints, in order to obtain a rough estimate of the conversion vertex position. This is then used as an input to the second vertex fit iteration where, in addition, an angular constraint is applied. This is based on the fact that the e^+e^- pair tracks are emerging parallel to each other at the vertex point being the decay products of a massless particle. This translates to an angular constraint $\Delta\phi = \Delta\theta = 0$ applied directly on the parameters of the two tracks considered resulting in an improved reconstructed vertex position resolution.

6.3.1 Vertex reconstruction efficiency and purity

The efficiency ($\mathscr{E}_{\text{vertex}}$) and purity ($\mathscr{P}_{\text{vertex}}$) of the vertex reconstruction are determined using the simulation. They are defined as follows:

$$\mathscr{E}_{\text{vertex}}(i) = \frac{\text{Number of events with} \geq 1 \text{ reconstructed vertex in layer } i}{\text{Number of events with two truth-matched tracks}}, \qquad (6.8)$$

$$\mathscr{P}_{\text{vertex}}(i) = \frac{\text{Number of events with a truth-matched conversion vertex in layer } i}{\text{Number of events with} \geq 1 \text{ reconstructed vertex}}, \qquad (6.9)$$

Figure 13 shows the vertex reconstruction efficiencies, both with and without the angular constraint, for each silicon tracker layer. As shown in figure 14, the purities are above 90 % except for the last three SCT layers. Again, as in the case of the track reconstruction, this is due to the presence of tracks from secondary photon conversions resulting in an increase of the combinatorial background.

Figure 15 shows the resolution of the x-position of the reconstructed vertices in the MC. The mean is offset by 6.5 mm due to biases during the vertex reconstruction when the two tracks share one or more of their silicon clusters closest to the conversion vertex. The reconstructed vertex position resolution is ~ 7.5 mm, fairly constant in the three pixel tracker layers relevant for the analysis presented here and significantly smaller to the clearances between the layers of the pixel and the SCT detectors of ~ 35 mm and ~ 70 mm, respectively. This allows for the observation of the structure of the individual silicon tracker layers. No corrections due to Bremsstrahlung losses on the reconstructed converted photon electron tracks have been applied. This results to the tail seen on the positive side of the reconstructed conversion vertex x-position resolution distribution in figure 15. Electrons from converted photons that have lost part of their energy due to bremsstrahlung effects, will bend more inside the magnetic field enveloping the tracker and will result therefore in the reconstructed conversion vertex position to be at larger values than it would have had otherwise. The tail on the negative side of the same distribution is due to the mis-reconstruction of conversion vertices where at least one of the participating tracks has missed one or more silicon hits. The effect is more pronounced the closer the missed silicon hits are to the reconstructed vertex position.

6.4 Conversion reconstruction efficiency

Not all reconstructed vertices correspond to converted primary photons. For example, electron tracks from secondary converted photons originating from Bremsstrahlung losses of the electrons from the primary converted photon, will produce some combinatorial background. The conversion reconstruction efficiency ($\mathscr{E}_{Conv}$) is again estimated using the simulation and refers to correctly reconstructed conversion vertices where both e^+e^--pair tracks are truth matched to the electrons produced from the primary converted photon. This can be expressed as:

$$\mathscr{E}_{Conv}(i) = \frac{\text{Number of events with a truth-matched conversion vertex in layer } i}{\text{Number of events with photon conversions in layer } i}. \qquad (6.10)$$

Figure 16 shows the conversion reconstruction efficiency as defined above. The efficiency is higher for early conversions than for late ones, as expected. This is due to the lower reconstruction efficiency of tracks originating late inside the silicon tracker because of the limited number of available silicon hits.
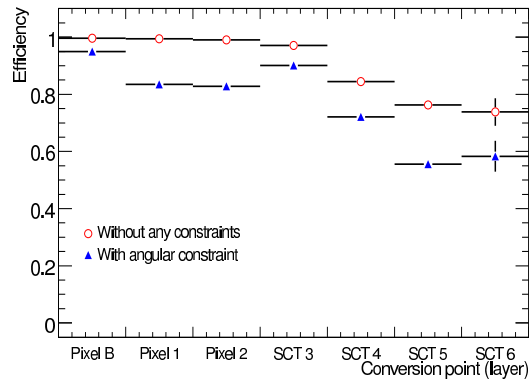
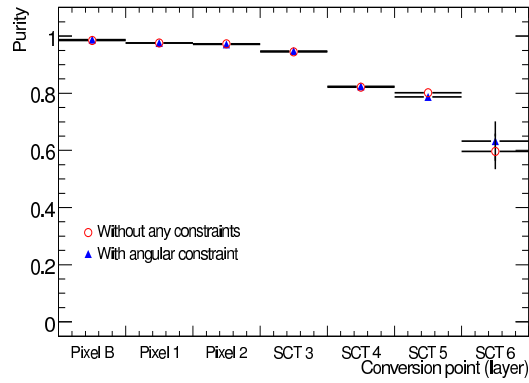**Figure 13**. Vertex reconstruction efficiency in each layer.
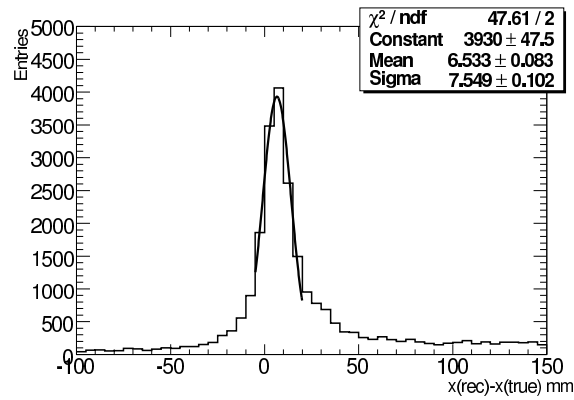

Figure 14. Reconstructed vertex purity in each layer.

Figure 15. Reconstructed vertex position resolution (see text for details).
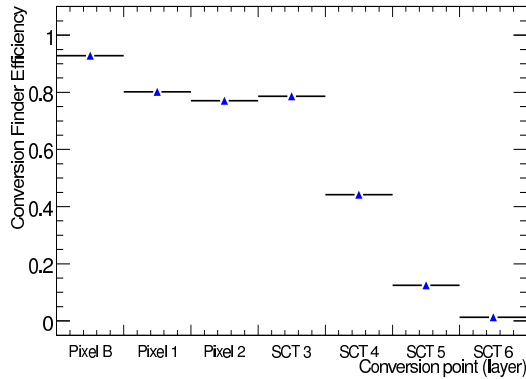
– 22 –

Figure 16. Conversion finder efficiency

7 Inner detector material estimation using photon conversions

The number of photon conversions is directly related to the amount of material in the tracker traversed by the beam photons. One can therefore use this information in order to estimate the amount of the material in the tracker, including passive material. This is extremely important since it directly relates to the quality of the electromagnetic calorimeter calibration and hence to the precision of its energy resolution. Appreciable effects can already be seen with $10\%X_0$ additional material in the tracker. The CTB experimental setup provides the opportunity of testing the possibility of using the conversion photons to measure the material in the tracker. Only an estimation of the material in the three pixel layers is made, due to the limited number of available converted photon statistics in the other layers. In order to reduce the uncertainties due to the number of incoming beam photons, a ratio of the estimated material in each pixel layer can be formed with respect to a reference volume where the material is well measured independently. In the CTB case this is provided by the copper foil placed 77 mm in front of the first pixel layer. Its thickness has been measured to be 37 μm. In the following, the estimation of the material in the copper foil and the three pixel layers is discussed in detail together with the corresponding statistical and systematic uncertainties. The small number of reconstructed photon conversions in the copper foil, does limit the overall precision that can be achieved by the CTB measurement to levels much higher than those desired for the precise energy calibration of the electromagnetic calorimeter, as it will be seen in the following sections. In the LHC collision environment this will not be the case due to the abundance of converted photons from π^0 or η decays in the minimum bias events. There a statistical precision of $< 2\%$ will be reached already with the first pb^{-1} of data and the measurement of the tracker material can be expanded to layers beyond those of the pixel system.

7.1 Description of the method

The amount of material (M) is measured by using the fraction of the photon conversions (F_{conv}) in a layer.

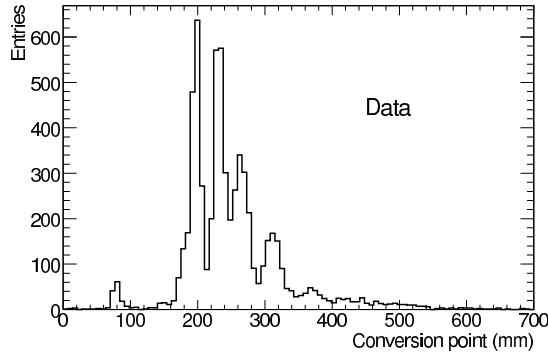$$M = -9/7 \cdot \ln(1 - F_{conv}) \tag{7.1}$$

– 23 –

Figure 17. Distribution of the reconstructed data vertex positions. The three pixel layers together with the copper foil in front are clearly distinguishable.

The conversion fraction F_{conv} is computed by the following expression;

$$F_{conv} = \frac{\text{Number of expected true conversions per layer in data}}{\text{Number of all incoming photons to the layer}}$$

$$= \frac{N_{rec}^{Data} \cdot P^{MC}/A^{MC}}{N_{all\gamma}^{Data} \cdot \exp(-7/9 \cdot M_{up})}. \tag{7.2}$$

where N_{rec}^{Data} is the number of reconstructed conversions on a specific detector layer, and $N_{all\gamma}^{Data}$ is the number of analyzed photons (in this analysis 308867 events where one event corresponds to one beam photon). Furthermore M_{up} is the total amount of the material upstream of each layer under consideration. Finally, P^{MC} is the correction factor due to background contamination, and A^{MC} is the correction to the signal vertices due to reconstruction inefficiencies. Both factors are estimated from the simulation.

$$P^{MC}(i) = \frac{\text{Number of vertices generated and reconstructed in layer } i}{\text{Number of vertices reconstructed in layer } i}, \tag{7.3}$$

$$A^{MC}(i) = \frac{\text{Number of vertices generated and reconstructed in layer } i}{\text{Number of vertices generated in layer } i}. \tag{7.4}$$

These correction factors will be described in more detail in section 7.2.1.

7.2 Number of reconstructed vertices

The distribution of the reconstructed conversion vertex positions for the full data sample is shown in figure 17. The structure of the pixel tracker is clearly visible becoming more difficult to resolve at larger distances due to the lower tracking efficiency. The small bump in front of the first pixel layer at ~ 77 mm, corresponds to the copper foil that was placed there. In order to count the number of reconstructed vertices in each layer, we need to determine the signal region. In figures 18 and 19, the vertex position distributions, in both the data and the simulation, are shown centered around

the copper foil and the pixel tracker area respectively. The small shoulder in front of the first pixel layer is due to the support box of the pixel tracker assembly. The corresponding vertex distributions for the data and the simulation are fitted with a function defined as follows,

$$F_{fit} = C_0 + \sum_{i=copper}^{Pixel2} a_i \times \exp\left(-\left(\frac{x - b_i}{c_i}\right)^2\right). \tag{7.5}$$

The above function matches well all of the distributions. The signal regions for the copper and for each pixel layer are then defined as the ones between the minima of the fit function. These are $x = 65 - 90$ mm for the copper, and $x = 180 - 215$ mm, $x = 215 - 250$ mm and $x = 250 - 290$ mm for each of the three pixel layers. In the case of the simulation the hatched histograms and the dashed histogram show the background contribution in each signal region obtained from the truth. This is due to either vertices wrongly reconstructed at the layer under consideration instead of at the layer immediately upstream, or, less often, to vertices reconstructed by a wrong combination of electron-positron tracks. Conversion vertices reconstructed at the wrong position result from poorly reconstructed tracks which missed at least one precision silicon hit close to the conversion vertex.

7.2.1 Efficiency (A^{MC}) and background (P^{MC}) correction per layer

In order to measure the efficiency correction, A^{MC} is separated into three components.

$$A^{MC} = A_{pre} \cdot E_{sel} \cdot E_{In}. \tag{7.6}$$

Each component shows the effect of each selection stage; A_{pre} is the efficiency during the pre-selection and is determined primarily by the geometrical acceptance. E_{sel} represents the efficiency of the vertex reconstruction. Finally, E_{In} is the efficiency for a reconstructed vertex to be within the selected signal region. The above variables are defined as follows:

$$A_{pre}(i) = \frac{\text{Number of generated vertices in layer } i \text{ that passed the pre-selection}}{\text{Number of generated vertices in layer } i}, \tag{7.7}$$

$$E_{sel}(i) = \frac{\text{Number of generated vertices in layer } i \text{ reconstructed after all selections}}{\text{Number of generated vertices in layer } i \text{ that passed the pre-selection}}, \tag{7.8}$$

$$E_{In}(i) = \frac{\text{Number of generated and reconstructed vertices after all selections in layer } i}{\text{Number of generated vertices in layer } i \text{ reconstructed after all selections}}. \tag{7.9}$$

Table 8 shows a list of the correction factors estimated by using the definition of the signal region described in section 7.2. The pre-selection is based on the information from the TRT and the LAr calorimeter as mentioned in section 6.2. A_{pre} is lower for layers farther from the TRT due to the larger probability for a conversion electron to bend in the magnetic field and end up outside of the geometrical acceptance of the detector. Both the background and the efficiency correction factors depend heavily on the definition of the signal region given that the pixel layers are close to each other.

7.3 Systematic uncertainties and material estimations

The statistical error is estimated from the final number of reconstructed vertices. The systematic uncertainties in this analysis are due to the geometrical acceptance, the selection procedure, the
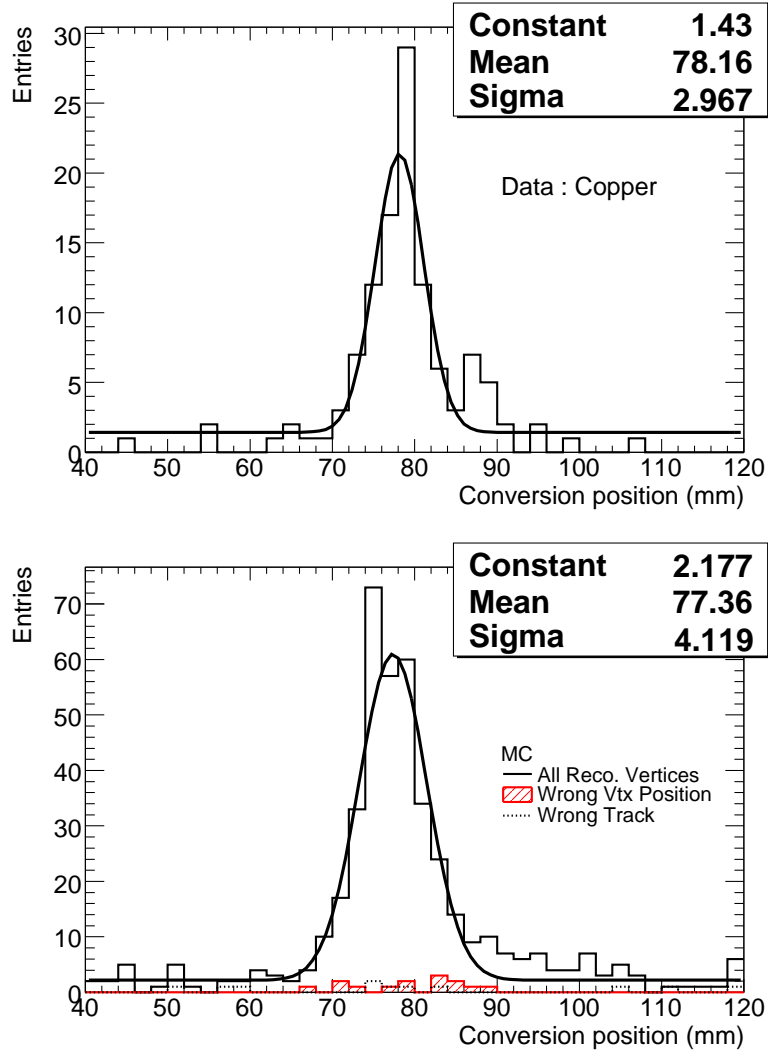
Figure 18. Reconstructed vertex position resolution for conversions on the copper foil. The simple gaussian fit indicates that the reconstructed position of the copper foil is within 1 mm from the one expected in the simulation. The shaded histogram indicates the background contribution due to vertices reconstructed at the wrong position whereas the dashed-line histogram the background contribution due to vertices where the track combination is wrong (see text for details).

definition of the signal region and the background correction. They are summarized in table 9 together with their effect on the estimated amount of the material in each layer. This is obtained by varying each one of A_{pre}, E_{sel}, E_{In} and P^{MC} individually within a range determined by the largest difference in their values seen in table 8 for all layers, and estimating the effect on deducing the corresponding amount of material in each layer. There is an important qualitative difference in the nature of the systematic uncertainties mentioned above. Those due to the geometrical acceptance and the reconstructed conversion vertex selection are largely correlated among the different pixel layers and the copper foil and will result in a coherent increase or decrease of the estimated amount
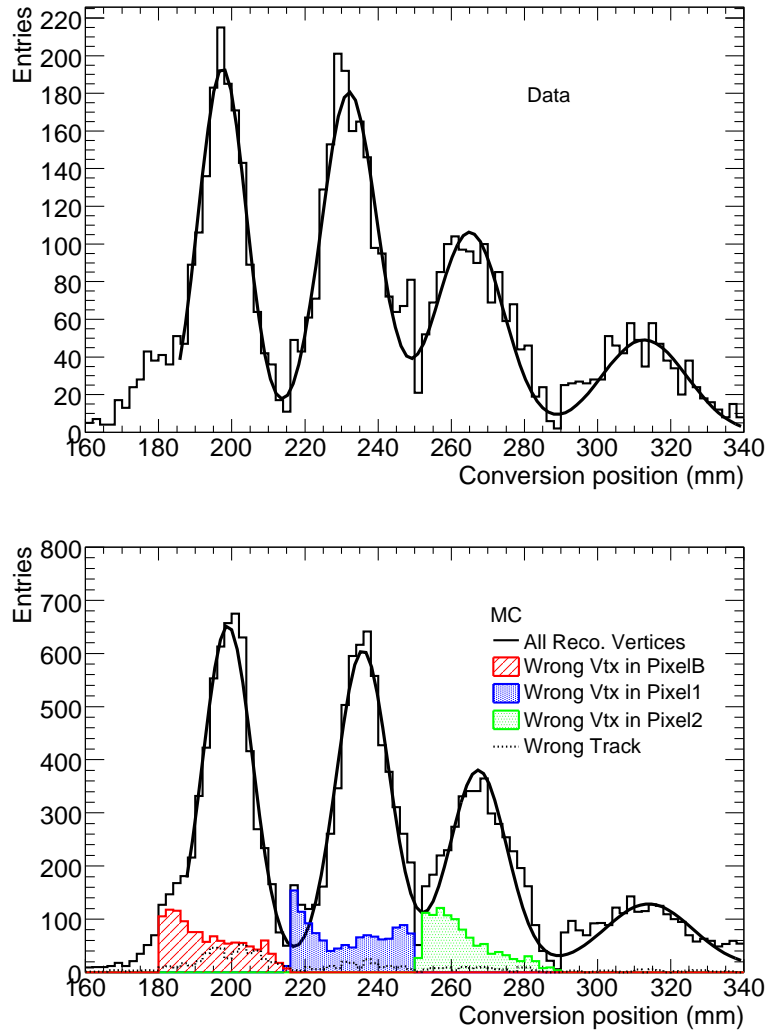
Figure 19. Reconstructed vertex position distribution for the three pixel Layers. The shaded histograms indicate the background contribution due to vertices reconstructed at the wrong position whereas the dashed-line histograms the background contribution due to vertices where the track combination is wrong (see text for details).

of the material on all layers. On the other hand the systematic uncertainties in the definition of the signal region and the background correction are layer-specific and taken to be uncorrelated among the different pixel layers and the copper foil. An additional source of systematic uncertainty is the poorly known incoming photon beam flux. One can use the reconstructed conversion vertices on the well measured copper foil for assigning an overall uncertainty to the material estimation due to the number of the incoming photons. By comparing the number of triggered incoming data photons to the one expected by counting the reconstructed converted photons on the copper foil assuming that we know the amount of material perfectly well, the difference is found to be $\sim 7\%$. This source of systematic uncertainty is in nature quite similar to the one due to the luminosity

Table 8. Summary of the correction factors (A_{pre}, E_{sel}, E_{In}, A^{MC} and P^{MC} for each layer)

	Data	MC							
Layer	Rec'ted	Signal	BG (Mig)	BG (comb)	A_{pre}	E_{sel}	E_{In}	A^{MC}	P^{MC}
Cu	121	330	15	7	46.3 ± 1.3	64.8 ± 1.8	75.7 ± 2.1	22.7 ± 1.1	93.8 ± 1.3
PixelB	1658	4296	1148	473	49.1 ± 0.4	74.2 ± 0.5	78.5 ± 0.6	28.6 ± 0.4	72.6 ± 0.6
Pixel1	1851	4368	1263	185	52.3 ± 0.4	69.9 ± 0.5	81.6 ± 0.5	29.8 ± 0.4	75.1 ± 0.6
Pixel2	1236	2913	1046	115	55.8 ± 0.4	51.0 ± 0.6	71.0 ± 0.7	20.2 ± 0.3	71.5 ± 0.7

Table 9. Relative error for X/X_0

for X/X_0	varied variable	Cu	PixelB	Pixel1	Pixel2
Geometrical acceptance	$\delta A_{pre}/A_{pre} \pm 9\%$	3.9%	4.0%	3.9%	4.0%
Vertex selection	$\delta E_{sel}/E_{sel} \pm 16\%$	11.4%	11.4%	11.2%	11.0%
Definition of signal region	$\delta E_{In}/E_{In} \pm 12\%$	8.0%	8.0%	8.2%	7.9%
Background subtraction	$\delta P^{MC}/P^{MC} \pm 14\%$	14.8%	15.0%	14.8%	14.9%
Photon Beam Flux	$\delta I/I \pm 7\%$	7.0%	7.0%	7.0%	7.0%
for $(X/X_0)/(X/X_0)_{Cu}$	varied variable				
Geometrical acceptance	$\delta A_{pre}/A_{pre} \pm 9\%$	—	0.02%	0.02%	0.03%
Vertex selection	$\delta E_{sel}/E_{sel} \pm 16\%$	—	0.0%	0.2%	0.4%
Definition of signal region	$\delta E_{In}/E_{In} \pm 12\%$	—	11.3%	11.4%	11.3%
Background subtraction	$\delta P^{MC}/P^{MC} \pm 14\%$	—	21.1%	20.9%	21.0%

quoted by collider experiments and will affect equally the material estimations on all pixel layers. By taking the ratio of the measured material of the three pixel layers to that of the copper foil one can completely eliminate the uncertainty due to the incoming photon beam flux and dramatically decrease the largely correlated ones due to the geometrical acceptance and the conversion vertex selection. This is also shown in the bottom half of table 9.

The final estimations of the amount of the material in the three pixel layers and the copper foil are shown in table 10. The ratio of the measured material in the three pixel layers to the one in the copper foil is also shown. There is good agreement with those from the simulation within the quoted statistical and systematic uncertainties.

8 Summary and conclusion

In this paper we have presented the results of the photon studies using the 2004 Combined Test Beam data. This is a combined analysis where both the electromagnetic calorimeter and the tracker data were used to study the response of the ATLAS sub-detectors to both converted and unconverted photons. The CTB data provide us with an excellent test stand for all the photon reconstruction

Table 10. Summary of the estimated amount of material for each layer

	Copper	PixelB	Pixel1	Pixel2
Reconstructed vertices	121	1658	1851	1236
X/X_0 (%) with errors	0.23±0.02±0.05	1.97±0.21±0.43	2.21±0.24±0.41	2.11±0.24±0.46
Ratio	—	8.57±1.25±2.05	9.61±1.43±2.29	9.17±1.39±2.19
X/X_0 (%) in MC	0.25	2.6	2.6	2.6
Ratio in MC	—	10.4	10.4	10.4

algorithms employed in the ATLAS experiment, which due to the lack of any other available data, have been designed, developed and tested using simulated data only.

The reconstruction of converted photons inside the ATLAS tracker is of particular importance. Due to the significant amount of material in the ATLAS tracker, on average $\sim 50\%$ of the photons will convert before reaching the cryostat of the electromagnetic calorimeter. Therefore efficient reconstruction of the converted photon signal is of paramount importance for any physics study that contains photons in its final state. We have shown that the existing reconstruction software utilizing the latest developments in both the tracking and the vertex reconstruction can achieve this goal. Clear identification of both converted and unconverted photons is important for the analysis of physics processes with photons as their final signatures since the converted and unconverted photons are characterized by different types of systematic uncertainties and can offer complementary ways in both extracting the signal and rejecting the background [12].

The identification of converted and unconverted photons using the full capabilities of the Liquid Argon calorimeter with a TRT-based tagging selection, allowed us to perform an accurate measurement of the difference in energy deposition between converted and unconverted photons of the same energy. Irrespective of the location of the conversion, be it early or late, a method has been developed that ensures identification by observing depositions in the presampler and first sampling of the calorimeter. This is possible thanks to the fact that photons converting early present a different longitudinal shower development, i.e. they initiate their showers earlier. While this study will eventually be repeated using the collected ATLAS data, the results presented here are for the moment the only quantitative measurement of the energy deposition difference between converted and unconverted photons. As such it has direct implications both in the energy calibration of the electromagnetic calorimeter and in developing data-driven algorithms for the measurement of the photon identification efficiency.

Of particular interest is also the use of the converted photons for mapping the material of the tracker with direct implications on the calibration scheme of the electromagnetic calorimeter. Among the different methods that have been proposed for estimating the amount of the material, the use of the photon conversions is particularly appealing. Through the reconstruction of the conversion vertex, they can provide in addition the precise location of the existing material. Under the controlled conditions of the Combined Test Beam where clean single photon beams were delivered, the method of using the converted photons to measure the tracker material has been first developed and tested. It is currently being employed for the mapping of the ATLAS tracker material using

the 2010 LHC data. Within the CTB framework, direct comparisons between the data and the expectations from the simulation can be made thus checking on the ability to use converted photons in order to locate the regions in the tracker where discrepancies may exist and correct for them. It has been found that the data agree well with the existing detector description in the simulation within a $\sim 20\%$ overall precision, due both to the rather low statistics and to the large systematic uncertainty stemming primarily from the inability, inherent in the CTB experimental setup, of accurately predicting the number of incoming photons. Both of the above will largely be absent during normal operations in a collision environment, resulting in a much improved material measurement precision. The first data acquired with the LHC beams more than support this last statement.

In conclusion the CTB data enable us to study important experimental aspects of the photon reconstruction. The results of two important applications where photons can be used have been presented. These are of particular interest for a number of on-going analysis efforts exploiting the 2010 data of the ATLAS detector at the LHC.

Acknowledgments

References

[1] ATLAS collaboration, G. Aad et al., *ATLAS liquid argon calorimeter: technical design report*, CERN-LHCC-96-41, CERN, Geneva Switzerland (1996).

[2] ATLAS collaboration, G. Aad et al., *The ATLAS experiment at the CERN Large Hadron Collider*, 2008 *JINST* **3** S08003.

[3] B. Di Girolamo et al., *Beamline instrumentation in the* 2004 *combined ATLAS testbeam*, ATLAS EDMS Note, ATL-TECH-PUB-2005-001, CERN, Geneva Switzerland (2005).

[4] M. Aharrouche et al., *Measurement of the response of the ATLAS liquid argon barrel calorimeter to electrons at the* 2004 *combined test-beam*, *Nucl. Instrum. Meth.* **A 614** (2010) 400.

[5] GEANT4 collaboration, S. Agostinelli et al., GEANT4*: a simulation toolkit*, *Nucl. Instrum. Meth.* **A 506** (2003) 250.

[6] B. Di Girolamo, M. Gallas and T. Koffas, 2004 *ATLAS barrel combined test beam layout*, ATLAS EDMS Note, ATC-TT-IN-0001, CERN, Geneva Switzerland (2005).

[7] T. Cornelissen et al., *Track fitting in the ATLAS experiment*, Ph.D. Thesis, University of Amsterdam, Amsterdam Netherlands (2006) [CERN-THESIS-2006-072].

[8] I. Gavrilenko, *Description of global pattern recognition program (xkalman)*, ATL-INDET-97-165, CERN, Geneva Switzerland (1997).

[9] ATLAS collaboration, G. Aad et al., *Expected performance of the ATLAS experiment, detector, trigger and physics: reconstruction of photon conversions*, CERN-OPEN-2008-020, CERN, Geneva Switzerland (2008), pg. 112.

[10] ATLAS ELECTROMAGNETIC BARREL CALORIMETER collaboration, M. Aharrouche et al., *Energy linearity and resolution of the ATLAS electromagnetic barrel calorimeter in an electron test-beam*, *Nucl. Instrum. Meth.* **A 568** (2006) 601 [`physics/0608012`].

[11] V. Kostyukhin, *Vkalvrt — a package for vertex reconstruction in ATLAS*, ATL-PHYS-2003-031, CERN, Geneva Switzerland (2003).

[12] CDF collaboration, D.E. Acosta et al., *Direct photon cross section with conversions at CDF*, *Phys. Rev.* **D 70** (2004) 074008 [`hep-ex/0404022`].